





Next generation of improved High Temperature Membrane Electrode Assembly for Aviation

Project funded by the Clean Hydrogen Partnership under the European Union Horizon Europe framework programme for Research & Innovation

EC Grant Agreement number: 101101407 Type of action: HORIZON JU - Research and Innovation Actions Work program topic addressed: HORIZON-JTI-CLEANH2-2022-03-08

Deliverable D4.4

Simulation of the electrochemical interface

WP4: New MEA development and manufacturing

Start date of project	01/01/2023	Duration	48 months
Lead beneficiary	CEA		
Due date of deliverable	31/12/2024	Actual submission date	30/01/2025

Type		
DATA	Data sets, microdata etc.	
DEC	Websites, patents filing, press & media actions, videos, etc.	
DEM	Demonstrator, pilot, prototype, plan designs	
DMP	Data Management Plan	
R	Document, report excluding the periodic and final reports x	
OTHER	Software, technical diagram, etc.	
Dissemination level		
PU	Public	X
SEN	Sensitive	

Funded by the European Union. Views and opinions expressed are however those of the author(s) only and do not necessarily reflect those of the European Union or Clean Hydrogen Partnership. Neither the European Union nor the granting authority can be held responsible for them.



Table of Contents

1		Execu	tive Summary	5
2		Preser	ntation of the models	6
	2.	.1 E	uROPIUM platform	6
		2.1.1	Channel code	6
		2.1.2	Rib-channel code: 2D version	8
		2.1.3	Rib-channel code: 1D version	11
	2.	.2 R	tib-channel and channel models equations	12
		2.2.1	Geometry and domains	12
		2.2.2	Physics and equations	13
3		Adapta	ation to high temperature and PBI membrane	27
		3.1.1	PBI membrane ionic conductivity	27
		3.1.2	Phosphoric acid properties in CL	27
4		Calibra	ation of the model parameters	32
	4.	.1 C	alibration methodology	32
		4.1.1	Step 0	33
		4.1.2	Step 1	33
		4.1.3	Step 2	33
		4.1.4	Step 3	33
		4.1.5	Step 4	33
		4.1.6	Notes	33
	4.	.2 C	Calibration of ECP and transport parameters	34
	4.	.3 C	Calibration of membrane ionic conductivity parameters	37
5		Preser	ntation of first results	38
	5.	.1 l-	V curve	38
	5.	.2 S	ome results	39
		5.2.1	RH	39
		5.2.2	Water content	40
		5.2.3	CL effective conductivity	41
		5.2.4	Electronic potential	42
		5.2.5	Ionic potential	44
		5.2.6	Overpotential	45
	5.	.3 P	EIS simulation	46
6		Conclu	usion and perspectives	47
7		Bibliog	graphy	48



Table of Figures

Figure 1: Perspective view. The simulation takes into account the physics (flow, electrochemistry) in th	ne
blue plane, parallel to the gas flow and perpendicular to the MEA plane. Orange and violet arrows sho	
the anode and cathode channel flows (case of counter-flow design). The dimensions on the picture do	
scale with real ones for visibility reasons.	
Figure 2: Cellule_2D lateral view: The blue-grey area is the simulated domain. Black lines denote	
interfaces between different materials. Red arrows correspond to channel flow orientation in case of	
counter-flow design. Orange arrows correspond to gas diffusion. The dimensions on the picture do no	ıt
scale with real ones for visibility reasons. The cell is symmetrical: the same components are present of	
both part of the membrane (though the properties may differ)	
Figure 3: Example of simulation result obtained with the Cellule_2D model for the local relative humidi	
Figure 4: Location of the 2D rib-channel modelled domain (area inside the red dashed line)	-
Figure 5: 2D rib-channel modelled domain	
Figure 6: AME_2D example of meshing. The same components are present on both part of the	9
membrane, but their properties are not necessarily identical (especially for the catalyst layers)	۵
Figure 7: Relative humidity field (left) and current densities (right): each solid lines corresponds to prof	
of current density along the longitudinal direction for one value of the average current density	
Figure 8: 1D-rib-channel code: simulated domain	
Figure 9: Geometry for the 2D channel model	
Figure 10: Geometry for the 2D rib-channel model	
Figure 11: Water content as a function of water activity	
Figure 12 : PA ionic conductivity as a function of water content	
Figure 13 : Surface coverage θ _{H3PO4} as a function of T and potential	
Figure 14: Experimental voltage vs. measured voltage @ 0.05 A/cm²	
Figure 15: Experimental voltage vs. measured voltage @ 0.5 A/cm²	
Figure 16 : Experimental voltage vs. measured voltage @ 1 A/cm²	
Figure 17 : Measured ohmic resistance vs simulated ohmic resistance	
Figure 18 : I-V curve for OC n°4 – Comparison between experiments and simulation	
Figure 19 : Evolution of RH in the MEA	
Figure 20 : Evolution of water content λ in CL and MB	
Figure 21 : Evolution of CL effective conductivity	
Figure 22 : Evolution of cathode electronic potential	
Figure 23 : Evolution of anode electronic potential	
Figure 24 : Evolution of ionic potential in the MEA	
Figure 25 : Evolution of overpotential at the CL cathode and CL anode	
Figure 26 : Evolution of local current density at the CL cathode and anode	45
Figure 27 : Impedance spectrum - CO n°4	
Figure 28 : Partial enlargement of the high frequency region	46
Table of Tables	
Table 1: Definitions of geometry and domains acronyms	13
Table 2: Experimental design for differential cell testing	32
Table 3: List of calibration parameters – EC and transport	34
Table 4: List of calibration parameters – membrane ionic conductivity	



Glossary

Abbreviation/ acronym	Description	
CL	Catalyst Layer	
EC / ECP	Electrochemical / Electrochemical Parameters	
GDE	Gas Diffusion Electrode	
GDL	Gas Diffusion Layer	
HOR	Hydrogen Oxidation Reaction	
нт	High Temperature	
IPM	Ion Pair™ Membrane	
МВ	Membrane	
MEA	Membrane Electrode Assembly	
MPL	Micro Porous Layer	
ос	Operating Conditions	
ORR	Oxygen Reduction Reaction	
PA	Phosphoric Acid	
РВІ	Polybenzimidazol	
PEIS	Potentiostatic electrochemical impedance spectroscopy	
PEM	Proton Exchange Membrane	
PEMFC	Proton Exchange Membrane Fuel Cell	
Pt	Platinum	
RH	Relative Humidity	



1 Executive Summary

This document describes the models used to simulate the electrochemical interface and the physics at the MEA scale, as part of Work Package 4 (WP4). It explains the models used, the adaptations to HT and to the presence of phosphoric acid, the calibration procedure and shows polarization curves, EIS and other results on differential cells.

The models are parametrized thanks to electrochemical data from WP3 and the structure of components and subcomponents characterized respectively in WP3 and Task 4.2

This document outlines the models adapted for this project.

Specificities of PBI membranes and membranes containing phosphoric acid were added and a calibration procedure was set up in order to reproduce the available experimental results.

The parameters obtained with the AME_1D models will be fed into the 2D models (rib-channel and channel) to enable more detailed simulations.

One will extract from the 1D models the contribution of the most limiting phenomena for performance.

The 2D models will, over a second phase, help in determining an optimal cell design.



2 Presentation of the models

PEMFC models have been developed at the CEA with the aim of:

Understand, validate and quantify the various phenomena that are supposed to take place within fuel cells,

identify the sources of performance losses, develop tools for sizing bipolar plates and MEAs.

As part of the NIMPHEA project, these models, designed for low-temperature fuel cells, have been extended to the cases of high-temperature fuel cells and adapted to take account of phosphoric acid in the electrode.

These models are developed in the CEA EuROPIUM model platform in the COMSOL Multiphysics commercial software. Matlab is used for building the models thanks to the COMSOL LiveLink Matlab scripting possibilities.

EuROPIUM is the acronym for *ElectRochemistry OPtImization Understanding Modeling framework*. It is a numerical platform including models at different scales to simulate fuel cell performances. The models calculate the physics and electrochemistry corresponding to a PEM-fuel cell:

2D Channel is a 2D model devoted to one channel, from inlet to outlet [1].
2D Rib-channel is a 2D model devoted to the simulation through cell of one rib + one channel on each

1D Rib-channel is a 1D version of this model that runs very quickly and so that can be used for parameter studies.

2.1 EuROPIUM platform

side. See description in [1].

2.1.1 Channel code

The **2D Channel model** (*i.e.*, Cellule_2D) is used to simulate the cell operation (see **Figure 1**) in a plane parallel to the channels. Ribs and channels are not distinguished here. This 2D plane spreads over the cathode and the anode excluding the bipolar plate.

It includes the channels, the GDLs and MEA: Figure 1.

In the simulated domain, the channel geometry is longer than the MEA part (**Figure 2**) in order to have an inlet establishment zone for velocity profile on both side.



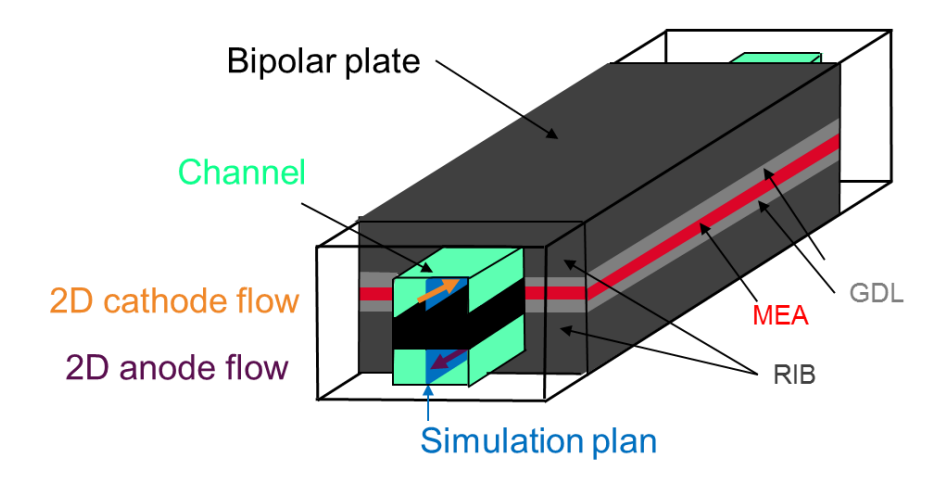


Figure 1: Perspective view. The simulation takes into account the physics (flow, electrochemistry) in the blue plane, parallel to the gas flow and perpendicular to the MEA plane. Orange and violet arrows show the anode and cathode channel flows (case of counter-flow design). The dimensions on the picture do not scale with real ones for visibility reasons.

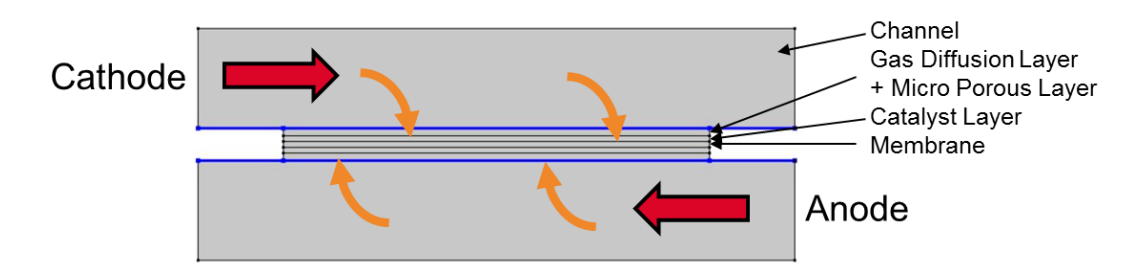


Figure 2: Cellule_2D lateral view: The blue-grey area is the simulated domain. Black lines denote interfaces between different materials. Red arrows correspond to channel flow orientation in case of counter-flow design. Orange arrows correspond to gas diffusion. The dimensions on the picture do not scale with real ones for visibility reasons. The cell is symmetrical: the same components are present on both part of the membrane (though the properties may differ)

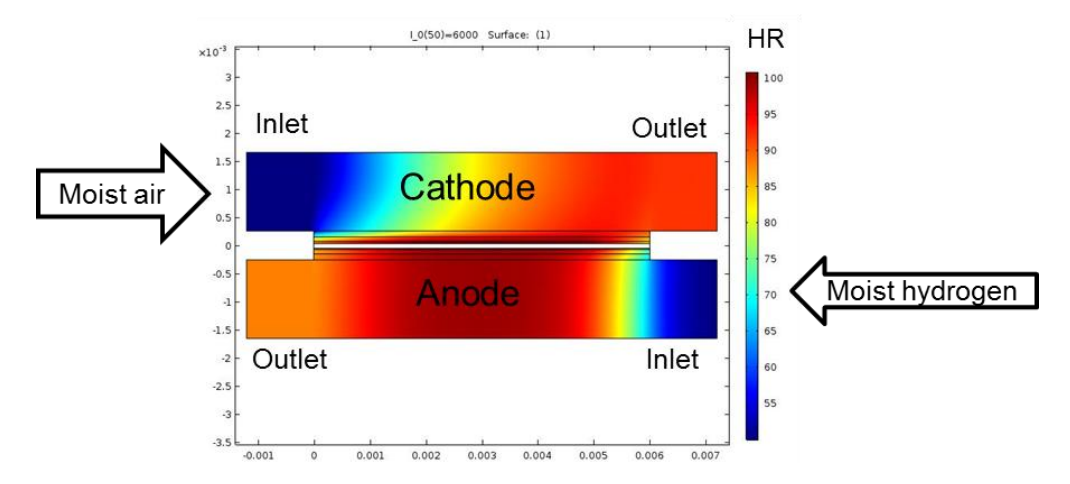


Figure 3: Example of simulation result obtained with the Cellule_2D model for the local relative humidity.



This model provides the longitudinal concentration evolution of the various species (oxygen, nitrogen, hydrogen, steam) profiles. It is sensitive to:

the inlet conditions: gas temperature, flux, humidity, the GDL and the MEA depth and their physical properties, the channel depth

It can be completed by the 2D rib-channel (i.e., AME_2D) model to have a more local insight.

Due to the high value of the ratio length to width, the refinement of the meshing leads either to a very high number of meshes or to a huge deformation of meshes. To bypass this problem the transport equations have been normalized. This normalization can be skipped if the mesh is structured.

The physical and electrochemical phenomena modelled are:

The Nernst and Butler-Volmer laws for the electrochemistry in the active layer.

A combination/modification of Stefan-Maxwell, Darcy and Fick laws ([2],[3],[4],[5],[6] and [7]) for the species transport inside the porous media (GDL, MPL): oxygen, nitrogen and steam on the cathode side; hydrogen and steam on the anode side.

When gas permeation is simulated, hydrogen and oxygen can cross the membrane but they are recombined into water in the catalyst layer of the other side of the membrane. Thus, the flow in the cathode channel does not contain any hydrogen and similarly, the anode flow does not contain oxygen. Diffusion of dissolved gases in ionomer (CL, membrane).

Diffusion and electro-osmosis of water in the membrane.

Darcy flow for the liquid water in the porous media (GDL, MPL).

Thermal conduction everywhere.

Ionic transport in the MPL and the membrane.

2.1.2 Rib-channel code: 2D version

The model is developed in Comsol Multiphysics and simulates the transport phenomena and electrochemistry in the MEA between two consecutives channels and through plane from anode to cathode as illustrated on the **Figure 4**. This code is often used with boundary conditions obtained from the **Channel code** simulations as explained farther.

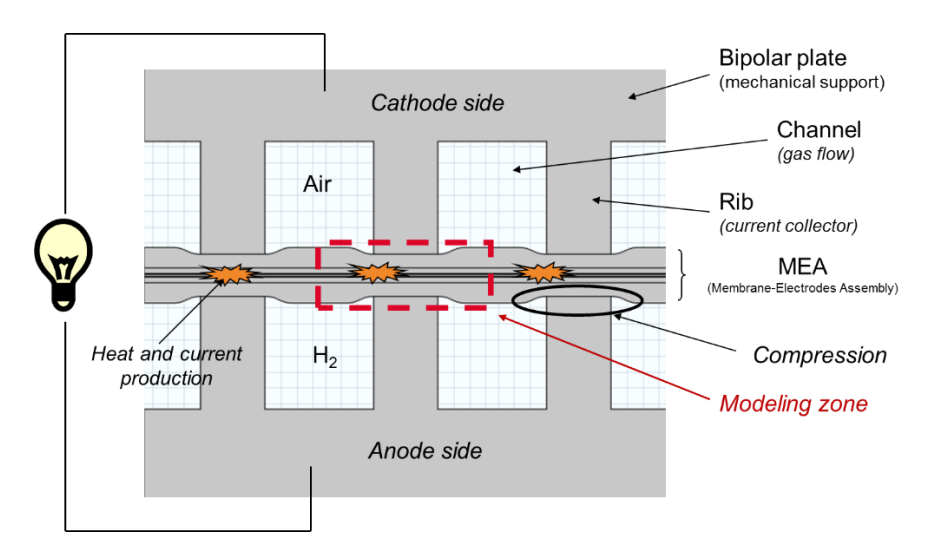


Figure 4: Location of the 2D rib-channel modelled domain (area inside the red dashed line).

The **Figure 5** below provides more details about the simulation domain such as the localization of the internal gas flux, the electrochemical reaction sites and the boundary conditions.



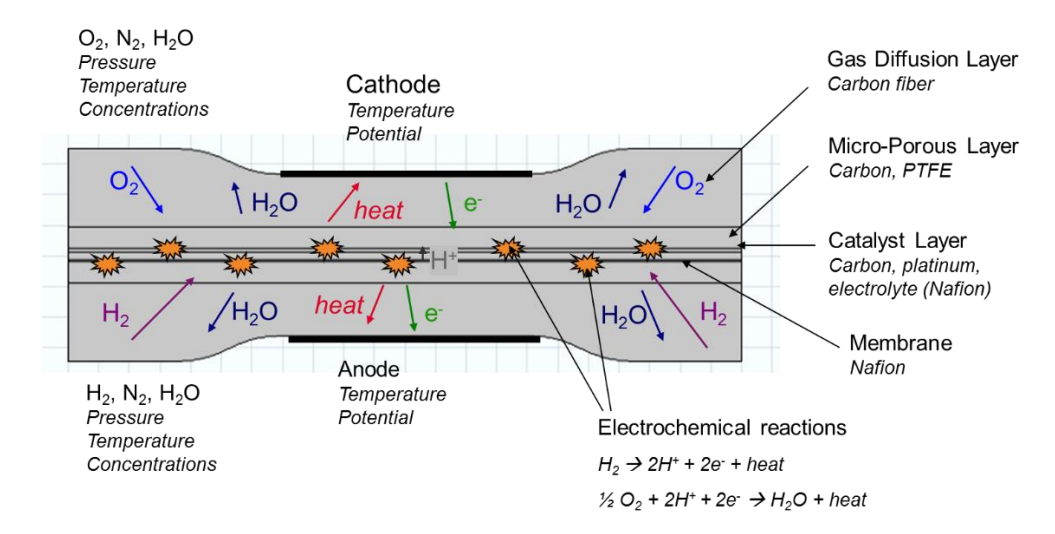


Figure 5: 2D rib-channel modelled domain

An example of meshing of the simulated domain using the Comsol interface is given on the **Figure 6**. The ribs have been included in the simulated domain in order to impose a uniform current density on the top the represented ribs thus, the current density profile on the rib/channel interface is obtained from simulation and not imposed which represents the reality in more realistic way.

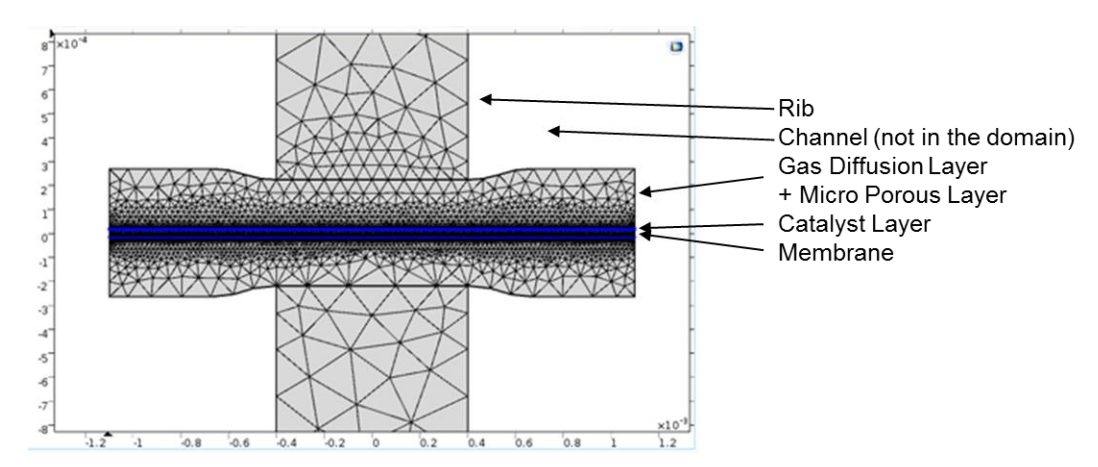


Figure 6: AME_2D example of meshing. The same components are present on both part of the membrane, but their properties are not necessarily identical (especially for the catalyst layers)



Some examples of results are given on the Figure 7:

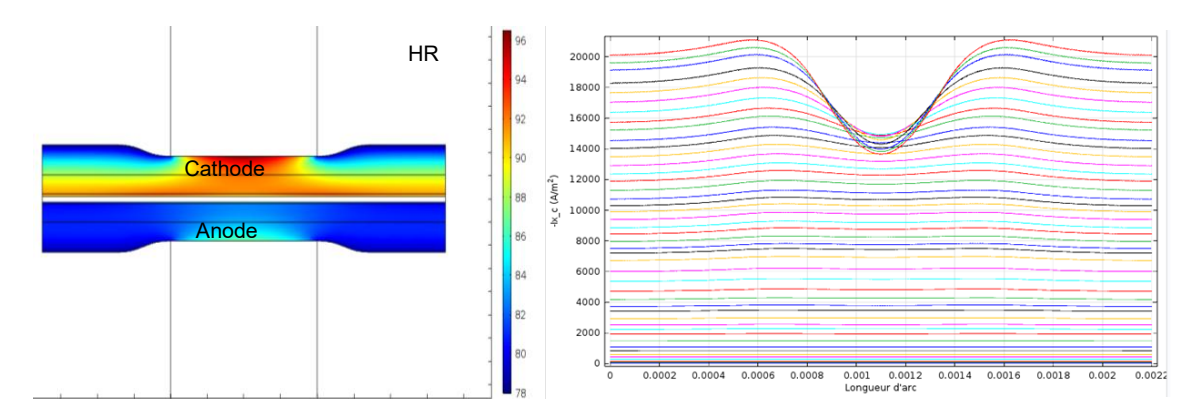


Figure 7: Relative humidity field (left) and current densities (right): each solid lines corresponds to profile of current density along the longitudinal direction for one value of the average current density

The physical and electrochemical phenomena modelled are:

The Nernst and Butler-Volmer laws for the electrochemistry in the active layer.

A combination/modification of Stefan-Maxwell, Darcy and Fick laws, as proposed by [7] for the species transport inside the porous media (GDL, MPL): oxygen, nitrogen and steam on the cathode side; hydrogen and steam on the anode side.

Diffusion of dissolved gases in ionomer (CL, membrane) [8].

Diffusion and electro-osmosis of water in the membrane and catalyst layer (in the ionomer) [9],[10],[11] and [12].

Optional Darcy flow for the liquid water [13] in the porous media (GDL, MPL, CL): usually not taken into account, works only in transient simulations.

Thermal conduction and convection in all the domains.

Ionic transport in the catalyst layer and the membrane.

NB:

In the same domains, the same equations are used for **Channel** and **Rib-channel** models.



2.1.3 Rib-channel code: 1D version

This model (i.e., AME_1D) is a geometric simplification of the AME_2D model.

It can be used for performing faster simulations, for example to fit the electrochemical parameters on experimental data.

The results are less accurate than those obtained with the AME_2D version, but when the rib/channel pattern is small and or when the current density is not too high (far from the diffusion limiting current), the rib/channel effect can usually be neglected.

The simulated domain is illustrated on Figure 8.

The main difference is in the boundary condition location: at the extremities of the domain, both the gas concentrations and the current are imposed at the same points.

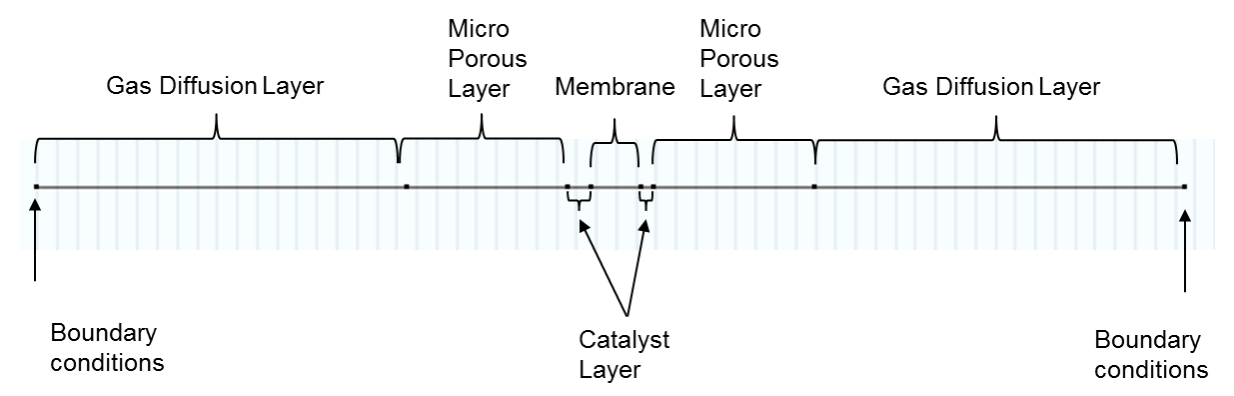


Figure 8: 1D-rib-channel code: simulated domain



2.2 Rib-channel and channel models equations

2.2.1 Geometry and domains

The Figure 9 corresponds to the simulation domain for the 2D channel model.

The Figure 10 corresponds to the simulation domain for the 2D rib-channel model.

The conventional notation is the following: domain names are in right character font, names of interfaces in italics and type of domain in orange.

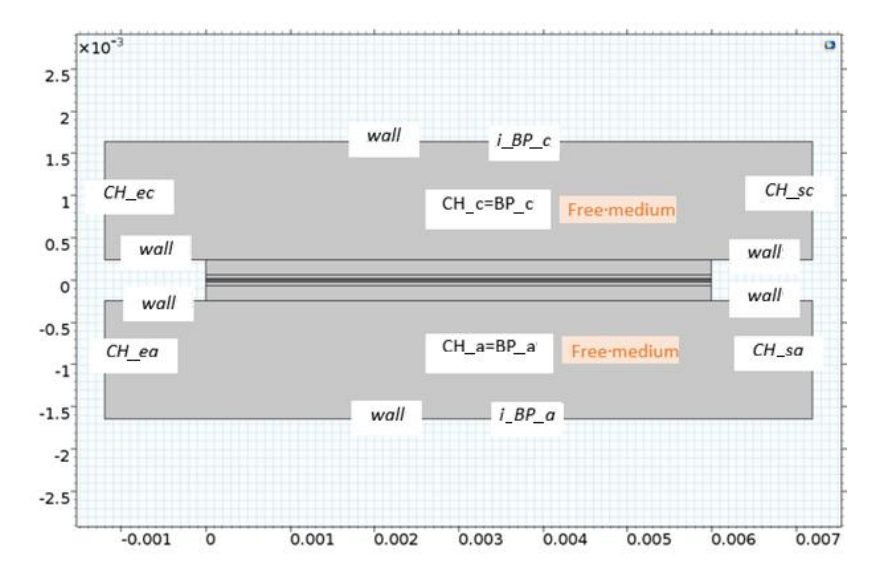


Figure 9: Geometry for the 2D channel model.

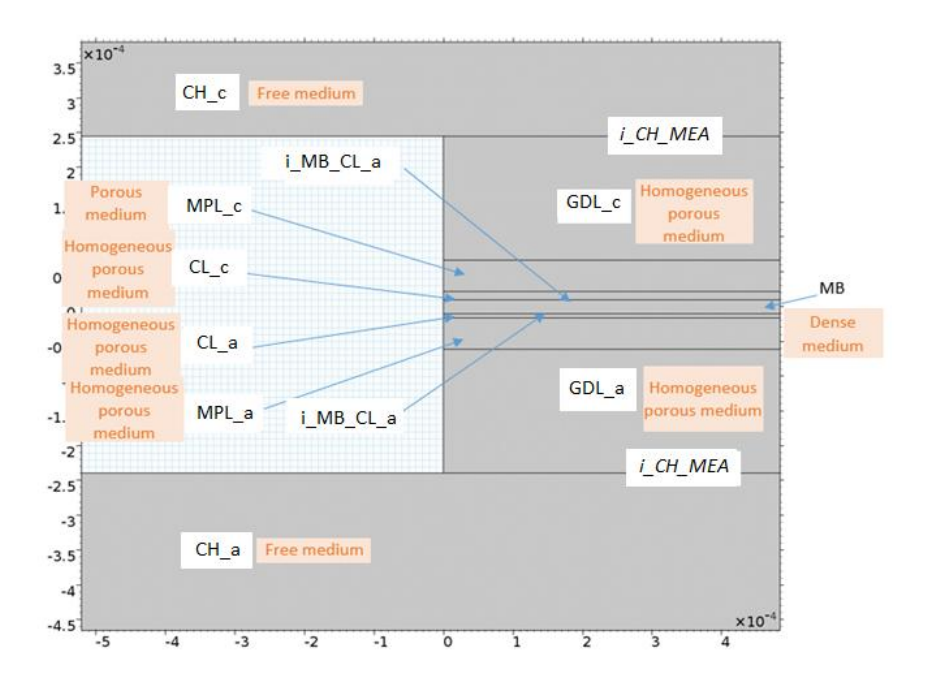


Figure 10: Geometry for the 2D rib-channel model

The table below defines the different acronyms used in the previous figures:



Table 1: Definitions of geometry and domains acronyms

Acronym	Definition
*_a	related to anode
*_c	related to cathode
*_ea / *_ec	anode/cathode inlet
*_sa / *_sc	anode/cathode outlet
i_	interface
BP	Bipolar plate
CH	Channel
MB	Membrane

2.2.2 Physics and equations

The conventional color notation for the equations is the following:

- the working (called "dependent") variables in red color are the main variables of the system
- those in orange are variables requiring closure from a physical model
- those in **green** are thermodynamic quantities to be determined from tables (distinction between orange and green is sometimes open to discussion).
- those in blue are constant or quantities calculated by the preprocessing.
- the vectors or matrix are denoted in **bold** characters.
- the scalar quantities and variables are in italics.

n is the normal vector at the boundary of a domain

2.2.2.1 Convection in the channels: Navier-Stokes

- Equations used to calculate the gas convection inside the channels. These equations deal with an averaged gas that have the properties calculated from all the gases involved. The net vaporization to condensation balance (S_{cond}) is considered: liquid water vaporized flux minus gas water condensed one.
- Domains : CH_a, CH_c
- Working variables : U V p
- Equations:
 - o Momentum balance is written as :

$$\rho_g \left(\frac{\partial \mathbf{u}}{\partial t} + \mathbf{u} \cdot \nabla \mathbf{u} \right) + M_v S_{cond} \mathbf{u} = -\nabla p + \nabla \cdot \left(\mu_g (\nabla \mathbf{U} + (\nabla \mathbf{U})^T) - \frac{2}{3} \mu_g (\nabla \cdot \mathbf{U}) \mathbf{I} \right)$$

Molar balance is written as:

$$\frac{\partial c_g}{\partial t} + \nabla \cdot (c_g \mathbf{U}) = S_{cond}$$

with:

 $\mathbf{u} = \begin{pmatrix} u \\ v \end{pmatrix}$, the mass average fluid velocity used in the left hand side terms of the momentum equation

 $\mathbf{U} = \begin{pmatrix} U \\ V \end{pmatrix}$, the volume (or molar) average fluid velocity (See also Memo-LMP-PS04)

 S_{cond} the vapor condensation rate

The two average velocities are related knowing the diffusion fluxes for the different species:



$$u = U + u_d$$

$$\mathbf{u_d} = \frac{\sum_i M_i \mathbf{N_i^d}}{\rho_a}$$

The total gases concentration depends on pressure and temperature:

$$c_g = \frac{P_g}{RT}$$

The total gases pressure is derived from the relative pressure used in the calculation:

$$P_q = p + P_0$$

Gases density and average molar mass depend on the composition:

$$\rho_g = c_g M_g$$

$$M_g = \sum_i X_i M_i$$

The viscosity of the gas mixture also depends on composition:

$$\mu_g = \sum_{i} \frac{X_i \mu_i}{\sum_{j} X_j \Phi_{ij}}$$

Where:

$$\Phi_{ij} = \frac{\left(1 + \sqrt{\frac{\overline{\mu_i}}{\mu_j}} {\left(\frac{M_j}{M_i}\right)}^{1/4}\right)^2}{\sqrt{8} \sqrt{1 + \frac{M_i}{M_j}}}$$

Boundary conditions at the boundaries listed below:

CH ea, CH ec: (inlet of the channels)

The gases volume velocity is imposed:

$$-U + u_0 \frac{c_{g,0}}{c_g} = 0$$
$$-V = 0$$

CH_sa, CH_sc: (outlet of the channels)

The pressure is imposed:

$$-\mathbf{n} \cdot \begin{pmatrix} -2\mu_g \frac{\partial \mathbf{U}}{\partial x} + \mathbf{p} \\ -\mu_g \left(\frac{\partial \mathbf{U}}{\partial y} + \frac{\partial \mathbf{V}}{\partial x} \right) \end{pmatrix} = \left(2\mu_g \frac{\partial \mathbf{U}}{\partial x} + \mathbf{p} \right) \cdot n_x + \mu_g \left(\frac{\partial \mathbf{U}}{\partial y} + \frac{\partial \mathbf{V}}{\partial x} \right) \cdot n_y$$

$$-\mathbf{n} \cdot \begin{pmatrix} -\mu_g \left(\frac{\partial \mathbf{V}}{\partial x} + \frac{\partial \mathbf{U}}{\partial y} \right) \\ -2\mu_g \frac{\partial \mathbf{V}}{\partial y} + \mathbf{p} \end{pmatrix} = \mu_g \left(\frac{\partial \mathbf{V}}{\partial x} + \frac{\partial \mathbf{U}}{\partial y} \right) \cdot n_x + \left(2\mu_g \frac{\partial \mathbf{V}}{\partial y} + \mathbf{p} \right) \cdot n_y$$

15 | Page

$$-\mathbf{p}=0$$

Walls:

Velocity is equal to zero at the walls of the channels:

$$-U = 0$$

$$-V = 0$$

i_CH_MEA:

Mass average velocity is constant across the MEA/Channel boundary:

$$-U + U_a^{GDL} = 0$$

$$-U + V_g^{GDL} = 0$$

2.2.2.2 Gas diffusion in channels: Stefan-Maxwell

- Equations used to calculate the diffusion of one gas in all the other gases inside the channels. All the gases are considered. Read [14],[4],[5] and [15].
- Domains: CH_a, CH_c
- Working variables: c_{X_2} c_{vap}
- Equations:

$$\frac{\partial c_i}{\partial t} + \nabla \cdot \left(\mathbf{N}_i^d + c_i \mathbf{U} \right) = S_{cond}$$

For
$$i = \{X_2, vap\}$$

With:

 $X_2 = H_2$ in the domain CH_a

 $X_2 = O_2$ in the domain CH_c

Diffusion flux N_i^d are calculated by solving the following equations:

$$c_g \nabla X_i = \sum_{i \neq i} \frac{X_i \mathbf{N}_j^d - X_j \mathbf{N}_i^d}{D_{ij}}$$

And

$$\sum_{i} \mathbf{N}_{i}^{d} = 0$$

for
$$i, j = \{X_2, N_2, vap\}$$

Note: this system of equations can be put in the form $c\nabla X = -A \cdot N$, with (for 3 species)

$$A = \begin{bmatrix} \frac{X_2}{D_{12}} + \frac{X_3}{D_{13}} & -\frac{X_1}{D_{21}} & -\frac{X_1}{D_{31}} \\ -\frac{X_2}{D_{12}} & \frac{X_1}{D_{21}} + \frac{X_3}{D_{23}} & -\frac{X_2}{D_{32}} \\ 1 & 1 & 1 & 1 \end{bmatrix}, N = \begin{bmatrix} N_1^d \\ N_2^d \\ N_n^d \end{bmatrix} \text{ and } c \nabla X = \begin{bmatrix} \nabla X_1 \\ \nabla X_2 \\ 0 \end{bmatrix}.$$

The system can then be inverted in the form $N = A^{-1} \cdot c\nabla X$.

By coupling with the balance equation we obtain:

$$\frac{\partial c}{\partial t} + \nabla \cdot (-A^{-1} \cdot c\nabla X + c U) = S_{cond}$$



With

$$c_{N_2} = c_g - (c_{X_2} + c_{vap})$$

$$S_{cond} = h_{cond}(c_{vap} > c_{sat})(c_{vap} - c_{sat})$$

$$c_{sat} = \frac{P_{sat}(T)}{P_q}$$

where $P_{sat}(T)$ is the vapor saturation pressure and S_{cond} the vapor to liquid water condensation rate. A heat production can be associated:

$$Q_{cond} = S_{cond} L_{\nu}(T)$$

The binary diffusion coefficients are taken from Transport Phenomena:

$$\begin{split} D_{H_2,N_2} &= \frac{2.46 \cdot 10^{-6} T^{2.334}}{P_g} \\ D_{O_2,N_2} &= \frac{6.43 \cdot 10^{-5} T^{1.823}}{P_g} \\ D_{H_2,vap} &= \frac{2.16 \cdot 10^{-5} T^{2.334}}{P_g} \\ D_{O_2,vap} &= \frac{4.26 \cdot 10^{-5} T^{2.334}}{P_g} \\ D_{N_2,vap} &= \frac{4.45 \cdot 10^{-6} T^{2.334}}{P_g} \end{split}$$

• Boundary conditions:

CH_ea, CH_ec:

$$-X_{X_2} + X_{X_2,0} = 0$$
$$-X_{van} + X_{van,0} = 0$$

with

$$X_i = \frac{c_i}{c_a}$$

i_CH_MEA:

$$\left(\mathbf{N}_i^d + c_i \mathbf{U}\right) - \mathbf{N}_i = 0$$



2.2.2.3 Gas diffusion in porous media: Young and Todd

- Equations used to calculate the motion of gases inside the porous media: the GDL and the MPL. The motion can results from both diffusion (several gases) and convection. Concerning steam, condensation and vaporization are taken into account (liquid vaporized flux minus steam condensed one).
- Domains: GDL_a, GDL_c, MPL_a, MPL_c, CL_a, CL_c
- Working variables : $c_{X_2} c_{N_2} c_{vap}$
- Equations

$$\begin{split} \epsilon \frac{\partial c_{X_2}}{\partial t} &= -\nabla \cdot \mathbf{N}_{X_2} - S_{X_2}^a \\ \epsilon \frac{\partial c_{N_2}}{\partial t} &= -\nabla \cdot \mathbf{N}_{N_2} - S_{N_2}^a \\ \epsilon \frac{\partial c_{vap}}{\partial t} &= -\nabla \cdot \mathbf{N}_{vap} + S_{H_2O}^d - S_{cond} + S_{evap} \end{split}$$

where the flux N_i are the solutions obtained from:

$$\frac{c_g \epsilon}{\mathbf{\tau}^2} \nabla X_i = \sum_{j \neq i} \left[\frac{X_i \mathbf{N}_j}{(D_A)_{ji}} - \frac{X_j \mathbf{N}_i}{(D_A)_{ij}} \right]$$

for
$$i = \{X_2, vap\}, j = \{X_2, N_2, vap\}$$

and

$$\frac{\epsilon}{\tau^2} \nabla P_g = -\mathbf{A}_{\mathbf{A}} \sum_i M_i^{1/2} \mathbf{N}_i$$

for
$$i = \{X_2, N_2, vap\}$$

Note: this last equation is equivalent to Darcy one when $D_i^k \sim \infty$ where the velocity is u_g defined hereafter. Note: in the cases that interest us, this system of equations of the form $\nabla c = A \cdot N$ can be inverted in the form $N = A^{-1} \cdot \nabla c$ if necessary to reveal a "multi-species diffusion tensor" A^{-1} .

$$X_2 = H_2$$
 in GDL_a, MPL_a, CL_a
 $X_2 = O_2$ in GDL_c, MPL_c, CL_c

$$\frac{1}{(D_A)_{ij}} = \frac{1}{D_{ij}} + \frac{1}{D_i^k}$$

$$\frac{1}{\mathbf{A_A}} = \frac{1}{\mathbf{A_C}} + \frac{1}{A_K}$$

$$D_i^k = \frac{2R_p}{3} \sqrt{\frac{8RT}{\pi M_i}}$$

$$A_K = \frac{3}{4R_p} \left(\frac{\pi RT}{2}\right)^{1/2}$$

$$\mathbf{A_C} = \frac{\varepsilon \mu_g}{c_g \mathbf{\tau}^2 \mathbf{K} K_{rg}(s) \sum_i X_i M_i^{1/2}}$$



Relative permeability [16]:

$$K_{rg}(s) = (1 - s)^3$$

Note: the parameters ϵ , τ , K, R_p are different according to the domains. In other versions of the model (which take into account deformations), they can also vary within a domain but these variations remain constant over time; they are therefore constant volume fields.

We define in addition (for the boundary condition with the channel):

$$\mathbf{U}_g = \begin{pmatrix} U_g \\ V_g \end{pmatrix} = \frac{\mathbf{N}_{X_2} + \mathbf{N}_{N_2} + \mathbf{N}_{vap}}{c_a}$$

Boundary conditions

i CH MEA:

$$-c_i + c_i^{CH} = 0$$

where $c_i^{\it CH}$ is the value of c_i in the domains CH_a and CH_c. Elsewhere:

$$\mathbf{N}_i \cdot \mathbf{n} = 0$$

<u>Note</u>: in the current resolution with COMSOL, the equations in porous media are everywhere the same and the physical properties of the porous medium vary from one domain to another. This is implicitly to impose continuity of flows and concentrations at the interfaces.

2.2.2.4 Dissolved species in the ionomer

- Diffusion flux of dissolved gases inside the membrane ([1], [17]) using Fick law.
- Species: Hydrogen, Nitrogen and Oxygen
- Domains:

CL_a, MB for H₂

CL c for O_2

CL_a, MB, CL_c for N₂

- Working variables : a_{H_2} a_{O_2} a_{N_2}
- Equations:

$$(1 - \epsilon)\epsilon_{ionomer}C_i^{ref} \frac{\partial a_i}{\partial t} = -\nabla \cdot (\mathbf{N}_i^a) + S_i^a + S_i$$

$$\mathbf{N}_i^a = -\mathbf{D}_{i,eff}^a C_i^{ref} \nabla a_i$$

$$C_i^{ref} = P_{ref}H_i^{ionomer}$$

$$\mathbf{D}_{i,eff}^a = \frac{(1 - \epsilon)\epsilon_{ionomer}}{\mathbf{\tau}_{ionomer}^2} D_i^a$$

Correction due to porosity and tortuosity is written as proposed by Epstein [18]. It can be noted that N_i^a , the in-plane diffusion in the ionomer of the CL is negligible compared to the diffusion in the gas (pores) phases. It is nevertheless kept in the model for numerical reasons (it avoids empty equations sets).



With, inside the domains CL a and CL c:

$$i = \{H_2, O_2, N_2\}$$

$$S_i^a = \gamma_{CL} h_i \left(C_i^{eq} - C_i \right)$$

 $C_i^{eq} = P_i H_i^{naf}$ ("naf" here, in accordance with the definition of h_i)

$$C_i = a_i C_i^{ref}$$

$$a_i^{eq} = \frac{P_i}{P_{ref}}$$

$$P_i = c_i RT$$

The thickness of the water and ionomer films are given by:

$$e_{water} = \frac{s\epsilon}{\gamma_c}$$

$$e_{ionomer} = \frac{(1 - \epsilon)\epsilon_{ionomer}}{\gamma_C}$$

where γ_{Pt} and γ_{C} are the developed surfaces of platinum and carbon in the catalyst layer (m²/m³_{CL}).

The global kinetic h_i is defined as:

$$h_i = \frac{H_i^{water}}{\frac{H_i^{ionomer}}{h_i^{water}} + \frac{H_i^{water}}{h_i^{ionomer}}}$$

$$h_i^{media} = \frac{1}{\frac{1}{k_i^{int,media}} + \frac{e_{media}}{D_i^{media}}}$$

A Henry's law is used at the ionomer/pore interface, with the coefficient:

$$H_i^{media} = k_0^H \exp(k_1^H \mathbf{a}_{H_2O}) \exp(k_T^H \left(\frac{1}{T} - \frac{1}{298.15}\right))$$

An interfacial absorption/desorption kinetic is used at the interface:

$$k_i^{int,media} = k_0^{int} \exp\left(k_1^{int} \mathbf{a}_{H_20}\right) \exp\left(-k_T^{int} \left(\frac{1}{T} - \frac{1}{298.15}\right)\right)$$

And a diffusion coefficient is used for the species in the ionomer:

$$D_i^{media} = k_0^D \exp(k_1^D \mathbf{a_{H_2O}}) \exp\left(-k_T^D \left(\frac{1}{T} - \frac{1}{298.15}\right)\right)$$

For the Nafion [1], [17], [19] and [20]:



	K _{H0}	K _{HT}	K _{D0}	k _{DT}
Hydrogen	3.8007e-04	1.0885e+03	4.1e-7	2602
Oxygen	1.0580e-04	707.2408	3.1e-7	2768
Nitrogen	6.4000e-06	1.3000e+03	4.24e-6	2246

In this (default) case $k_{H1}=0$, $K_{D1}=0$, $k_{int0}=1$, $k_{int1}=0$, $k_{int1}=0$ ($k_{int0}=1$ is a very high value, so that interfacial kinetic is not a limiting phenomena).

Boundary conditions

 $\mathbf{N}_{N_2}^a \cdot \mathbf{n} = 0$ for all external interfaces

 $\mathbf{N}_{02}^{a} \cdot \mathbf{n} = 0$ for all external interfaces

 $\mathbf{N}_{H_2}^a \cdot \mathbf{n} = 0$ for all external interfaces, except at i_MB_CL_c where $C_{H_2} = 0$

2.2.2.5 Water in the ionomer

• Motion of water inside the membrane due to diffusion and electro-osmosis.

• Domains : CL_a, MB, CL_c

• Working variables: a_{H_20}

Equations

Molar species balance:

$$(1 - \epsilon)\epsilon_{ionomer}C_{SO3} - \lambda' \frac{\partial a_{H_2O}}{\partial t} = -\nabla \cdot \left(\mathbf{N}_{H_2O}\right) - S_{H_2O}^d + S_{H_2O} - (1 - \epsilon)\epsilon_{ionomer}\lambda \frac{\partial C_{SO3}}{\partial t}$$

$$\mathbf{N}_{H_2O} = n_d \frac{\mathbf{I}_i}{F} - \mathbf{D}_{w,eff}(C_{SO3} - \lambda' \nabla a_{H_2O} + \lambda \nabla C_{SO3} -)$$

$$\lambda = f_{\lambda}(a_{H_2O}), \lambda' = f'_{\lambda}(a_{H_2O})$$

Diffusion [12], [21] and [22]:

$$D_{w} = k_{0}^{D_{w}} \left(1 + k_{1}^{D_{w}}\right) \exp\left(-k_{T}^{D_{w}} \left(\frac{1}{T} - \frac{1}{298.15}\right)\right)$$

$$\mathbf{D}_{w,eff} = \frac{(1 - \epsilon)\epsilon_{ionomer}}{\mathbf{\tau}_{ionomer}^{2}} D_{w}$$

Electro-osmosis [9]:

$$n_d = k_0^d + k_1^d \frac{\lambda}{\lambda} + k_2^d \frac{\lambda^2}{\lambda^2}$$

For Nafion : k_0^d =1, k_1^d =0.028, k_2^d =0.0026

In the domains CL_a, CL_c [1], [11], [21] and [23]:

$$S_{H_2O}^{d} = h_{H_2O} \gamma_{CL} C_{SO3} - \left(\lambda - f_{\lambda} \left(\alpha_{H_2O}^{eq}\right)\right)$$

The overall absorption/desorption kinetic is given by:



$$h_{H_2O} = \frac{1}{\frac{1}{k^{int}} + \frac{D_w}{e_{innomer}}}$$

The interfacial absorption/desorption kinetic is given by:

$$k^{int} = k_0^{int} \exp\left(-\frac{k_T^{int}}{RT}\right)$$

The water sorption isotherm for Nafion is for example given by:

$$f_{\lambda}(a_{H_20}) = 0.043 + 17.81 a_{H_20} - 39.85 a_{H_20}^2 + 36 a_{H_20}^3$$

Concentration, activity and partial pressure are defined:

$$C_{H_2O} = \lambda C_{SO3}$$

$$a_{H_2O}^{eq} = \frac{P_{vap}}{P_{sat}(T)}$$

$$P_{vap} = c_{vap}RT$$

Water in ionomer is considered as liquid in terms of enthalpy, so a heat consumption has to be associated with desorption (as water is considered appearing in vapor form in the pores):

$$Q_{H_2O}^d = -S_{H_2O}^d \mathbf{L}_v(T)$$

• Boundary conditions:

$$\mathbf{N}_{H_2O} \cdot \mathbf{n} = 0$$

<u>Takin into account the ionomer swelling in the catalyst layer:</u> computation of the resulting porosity in the catalyst layer and sulfonic sites concentration.

Considering the dry ionomer, the volume of the pores, ionomer and carbon+platinum can be expressed:

$$V_{por}^{dry} = \epsilon^{dry} V$$
 $V_{ionomer}^{dry} = \epsilon^{dry}_{ionomer} (1 - \epsilon^{dry}) V$
 $V_{CPt} = (1 - \epsilon^{dry}_{nat}) (1 - \epsilon^{dry}) V$

Taking into account the swelling, we have:

$$V_{por} = \epsilon V$$

$$V_{ionomer} = r_{naf} \epsilon_{naf}^{dry} (1 - \epsilon^{dry}) V$$



where $r_{naf}=1+\lambda \frac{M_{H_2O}}{EW}\frac{\rho_{dry}}{\rho_{lig}(T)}$ is the swelling ratio of the ionomer

As $V_{por} = V - (V_{naf} + V_{CPt})$, the wet porosity and volume fraction of ionomer in the solid phase can be extracted:

$$\epsilon = 1 - (1 - \epsilon^{dry}) \left(1 + \epsilon^{dry}_{naf} (r_{naf} - 1) \right)$$

$$\epsilon_{naf} = \frac{r_{naf} \epsilon^{dry}_{naf}}{1 + \epsilon^{dry}_{naf} (r_{naf} - 1)}$$

2.2.2.6 Ionic transport

- Protonic conduction inside the membrane and the catalyst layers.
- Domains: CL_a, CL_c, MB
- Working variable: Φ
- Equations

Domains CL_a, CL_c:

$$C_{dl} \frac{\partial \Phi}{\partial t} + \nabla \cdot \mathbf{I}_{i} = i_{e} + C_{dl} \frac{\partial \Psi}{\partial t}$$

Domain MB:

$$\nabla \cdot \mathbf{I}_i = 0$$

with

$$\mathbf{I}_i = -\mathbf{\kappa}_{eff} \cdot \nabla \Phi$$

where [9], [18] and [21]:

$$\mathbf{\kappa}_{eff} = \frac{(1 - \epsilon)\epsilon_{ionomer}}{\mathbf{\tau}_{ionomer}^2} \kappa$$

Heat production is associated with ohmic losses (Joule effect):

$$Q_i^{joule} = -\mathbf{I}_i \cdot \nabla \Phi$$

The ionic conductivity is given by [9], [18] and [21]:

$$\kappa = k_1 (\lambda - k_3)^{k_2} e^{k_T \left(\frac{1}{T_0} - \frac{1}{T}\right)}$$

• Boundary conditions

$$\mathbf{I}_i \cdot \mathbf{n} = 0$$



2.2.2.7 Electrical transport

- Electric conduction inside all the solid materials except the membrane.
- Domains: BP_a, BP_c, GDL_a, GDL_c, MPL_a, MPL_c, CL_a, CL_c
- Working variable: Ψ
- Equations

Domains CL_a, CL_c:

$$C_{dl} \frac{\partial \Psi}{\partial t} + \nabla \cdot \mathbf{I}_{e} = -i_{e} + C_{dl} \frac{\partial \Phi}{\partial t}$$

Other domains:

$$\nabla \cdot \mathbf{I}_e = 0$$

With

$$I_e = -\sigma_{eff} \cdot \nabla \Psi$$

Heat production is associated with ohmic losses (Joule effect):

$$Q_e^{joule} = -\mathbf{I}_e \cdot \nabla \Psi$$

Boundary conditions

i_BP_a:

$$\Psi = 0$$

i_BP_c:

$$I_e \cdot \mathbf{n} = I_0$$

i_MB_CL_a and i_MB_CL_c and everywhere else:

$$\mathbf{I}_e \cdot \mathbf{n} = 0$$

<u>Note</u>: the boundary conditions between "internal" domains are not expressed because they are implicitly taken into account in the COMSOL calculation but they correspond to conditions of continuity of the flow and the value.



2.2.2.8 Thermal heat transfer

- Heat equation based on the Fourier's law. The heat is generated inside the catalyst layer where the electrochemical reaction takes place. The heat is release to the cooling circuit through the MPL, the GDL and the channels. Only the conduction and the balance on the solid parts are taken into account in the current implementation.
- Domains: all
- Working variable : T
- Equations

$$\epsilon \left(\rho c_p + \sum c_i C_{pi} \right) \frac{\partial T}{\partial t} + \nabla \cdot \left(-\lambda \cdot \nabla T \right) = Q_{conv} + Q_{reac} + Q_{perm} + Q_{H_2O}^d + Q_e^{joule} + Q_i^{joule} + Q_{cond/evap}^{joule}$$

where Q_{conv} is the heat transport related to convection of the species :

$$Q_{conv} = -\sum \nabla H_i(T) \cdot \mathbf{N}_i$$

Boundary conditions:

i_BP_MEA:

$$T = T_0$$

Elsewhere:

$$-\lambda \cdot \nabla T = 0$$

2.2.2.9 Electrochemistry

- Calculation of the potential and current density inside the catalyst layer where the electrochemical reactions takes place. Calculation of the Nernst ([24], [25] and [26]) potential (E_{rev}). Calculation of the current density i_r as function of the overpotential using the Butler-Volmer equation. The over-potential η is function of the electrical and ionic potentials and the reversible potential. The exchange current density i_0 involved in the Butler-Volmer relation is function of the species activities a_i and the kinetic rates k. See also memo LMP-PS01 and LMP-PS02.
- Domains : CL_a, CL_c
- Working variable: none ("closure" relationships only)
- Equations.

Butler-Volmer formulation	"Direct kinetics" formulation
$E_{rev} = -\frac{\Delta G^{\circ}}{nF} + \frac{RT}{nF} \log \left(\prod_{i} a_{j}^{v_{j}} \right)$	$v_{ox} = k_{ox} \exp\left(\frac{\alpha nF}{RT}E\right)$
$i_r = i_0 \gamma_{Pt} \left[\exp\left(\frac{\alpha nF}{RT} \eta\right) - \exp\left(-\frac{(1-\alpha)nF}{RT} \eta\right) \right]$	$v_{red} = k_{red} \exp\left(-\frac{(1-\alpha)nF}{RT}E\right)$
$\eta = (\Psi - \Phi) - E_{rev}$	$E = \Psi - \Phi$ $k_{ox} = k_{ox}^{\circ} \prod_{v_{i} > 0} a_{j}^{v_{j}}$
$i_0 = i_0^{\circ} \left(\prod_{\nu_j > 0} a_j^{\nu_j} \right)^{1-\alpha} \left(\prod_{\nu_j < 0} a_j^{-\nu_j} \right)^{\alpha}$	$k_{red} = k_{red}^{\circ} \prod_{j=0}^{n-\gamma_j} a_j^{-\gamma_j}$
$i_0^{\circ} = nF(k_{ox}^{\circ})^{1-\alpha} (k_{red}^{\circ})^{\alpha}$	v̄ _j <0
	$i_r = nF(v_{ox} - v_{red})$



Note:

The difference between the two methods lies in their mathematical formulations.

The "classical" formulation of Butler-Volmer has an analytical interest as it highlights overpotential and equilibrium potential (Nernst).

The direct formulation is valuable because it remains applicable when there is no equilibrium (for example, when there is no more O_2 or H_2). It is slightly more numerically robust (and not more difficult to implement). However, when the reaction orders are changed (and are no longer equal to the stoichiometric coefficients of the reaction), the models are no longer entirely equivalent.

By default, the reaction order γ_j is considered equal to the stoichiometric coefficient ν_j of the reaction. This is thermodynamically consistent and supposedly true for an elementary reaction. Now, as HOR and especially ORR, are far from elementary electrochemical reaction, the reaction order (for the reactant and products) is usually fitted on experimental results.

$$k_{ox}^{\circ} = k^{\circ} T \exp\left(-\frac{\Delta G_{ox}^{*}}{RT}\right) \quad k_{red}^{\circ} = k^{\circ} T \exp\left(-\frac{\Delta G_{red}^{*}}{RT}\right)$$

$$k^{\circ} = \frac{k_{B}}{s_{0} N_{A} h}$$

where is k_B the Boltzmann constant, s_0 the average atomic surface of the platinum, N_A the Avogadro number and h the Planck constant. The Gibbs activation energies are decomposed as:

$$\Delta G_{ox}^* = \Delta H_{ox}^* - T \Delta S_{ox}^*$$
$$\Delta G_{red}^* = \Delta G^{\circ} + \Delta G_{ox}^*$$

where $\Delta G^{\circ} = \Delta H^{\circ} - T \Delta S^{\circ}$ is the reaction free enthalpy at reference pressure P_{ref} , but actual temperature. The reactions enthalpy and entropy ΔH° and ΔS° are computed from the thermodynamical data [27] for the involved species.

Heat production:

$$Q_{reac} = \left((\Psi - \Phi) + \frac{\Delta H^{\circ}}{nF} \right) i_e$$



For each electrode, these equations lead to:

Domain: CL_a

$$i_e = i_r$$
 $i_0 = i_0^* a_{H_2}^{(1-\alpha_a)\gamma_{H_2}} a_{H^+}^{\alpha_a\gamma_{H^+}}$
 $S_{H_2} = -\frac{i_r}{2F}$
 $S_{N_2} = 0$
 $S_{H_2O} = 0$

Domain: CL_c

$$i_e = i_r + i_p$$
 $i_0 = i_0^* a_{02}^{\alpha_c \gamma_{O2}} a_{H^+}^{\alpha_c \gamma_{H^+}} a_{H_2 O}^{(1 - \alpha_c) \gamma_{H_2 O}}$
 $S_{O_2} = \frac{i_r}{4F}$
 $S_{N_2} = 0$
 $S_{H_2 O} = -\frac{i_r}{2F}$
 $i_p = \frac{I_p}{e_{CL_c}}$

With I_p taken at the interface i_MB_CL_c:

$$I_p = 2FN_{H_2}^a \cdot \mathbf{n}$$

(where n is the membrane/catalyst layer interface normal vector)

A heat source is caused by the permeation current:

$$Q_{perm} = -\frac{\Delta H_a^{\circ} + \Delta H_c^{\circ}}{nF} I_p$$

The electrochemical equations can also be written in "direct" form (without introducing the reversible potential and the exchange current density) as described in [10] and [11].

Note: The density of active sites is assumed to be homogeneous throughout the volume of the catalyst layer. The model does not take into account any specific structure or organisation of the Pt nanoparticles within the CL and therefore of the catalytic sites. The distribution of catalyst sites is assumed to be homogeneous throughout the thickness of the CL. Heterogeneities in distribution could occur at the nanometre scale and differences in structure at the atomic scale. The heterogeneity in the distribution at the nanometre scale will affect the local transport limitations. The structure of the catalytic site should primarily change its activity. This implies that all the electrochemical and transport parameters estimated by fitting the experimental data to the model are averaged values.



3 Adaptation to high temperature and PBI membrane

There are several steps involved in adapting PEM models to HT:

ensuring the validity of the various correlations and laws used: gas diffusion coefficients, fluid viscosities, material properties;

replacing the properties of the electrolytes used at low temperatures with those of PBI membranes and phosphoric acid.

The properties required for the simulation are taken from the bibliography (see section 7).

3.1.1 PBI membrane ionic conductivity

The conductivity of PBI membranes was measured by Q.F. Li, H.C. Rudbeck, A. Chromik, J.O. Jensen, C. Pan, T. Steenberg, M. Calverley, N.J. Bjerrum, J. Kerres, "Properties, degradation and high temperature fuel cell test of different types of PBI and PBI blend membranes", Journal of Membrane Science, Volume 347, Issues 1-2, 2010, Pages 260-270.

This conductivity is modelled by a law of the form :

$$\sigma = k_1 (RH - k_3)^{k_2} \exp\left(k_T \left(\frac{1}{303.15} - \frac{1}{T}\right)\right)$$

which has been calibrated on the experimental points (see section 4).

3.1.2 Phosphoric acid properties in CL

The modifications concern the properties of the PA in the active layers: composition and conductivity as a function of RH and oxygen diffusion coefficient through a PA film.

Two articles were used:

that of Melchior et al. [28], which proposes a formalism for PA very similar to that used for ionomer in PEMFCs. The authors introduce the concept of water content (λ), which makes it possible to establish a link between RH (or water activity) and the ionic conductivity of phosphoric acid. That of Scharifker [29], who measured the solubility and diffusion of oxygen in PA.



3.1.2.1 Water content of PA in CL

The sorption isotherm for phosphoric acid is as illustrated in **Figure 11** (equilibrium water content as a function of water activity), according to Melchior [28]:

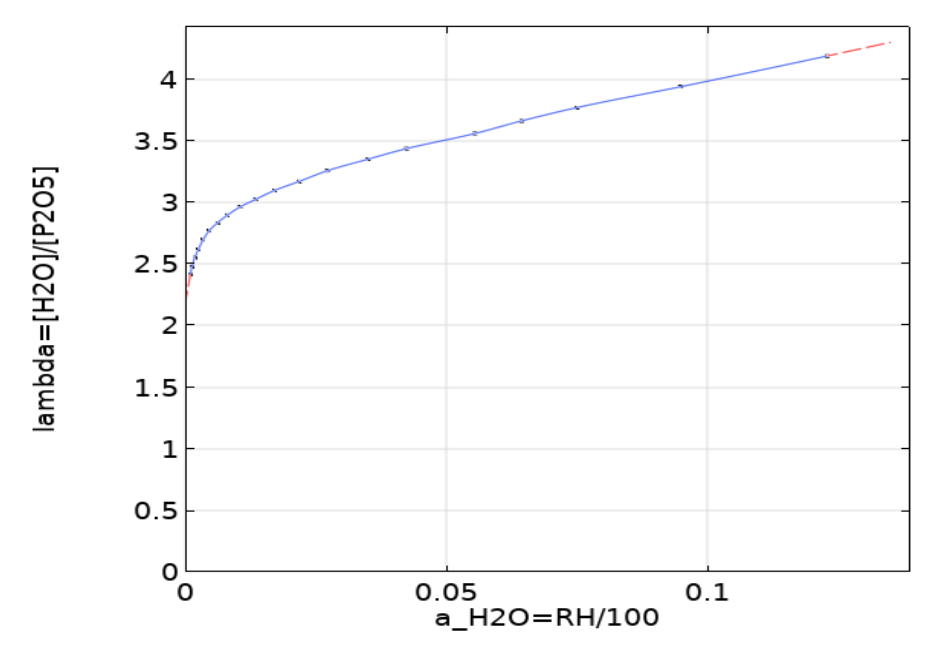


Figure 11: Water content as a function of water activity

The water concentration (in mol/m³) is defined as a function of the water content loading λ by:

$$C_{H2O} = \frac{1}{\frac{M_{H2O}}{\rho_{liq}} + \frac{1}{\lambda_{H3PO4}} \frac{M_{H3PO4}}{\rho_{H3PO4}}}$$

With:

$$\lambda_{H3PO4} = \frac{\lambda_{P2O5} - 3}{2}$$

$$\lambda_{P2O5} = \lambda = [H_2O]/[P_2O_5]$$

Mass fractions are defined by:

$$w_{H3PO4} = \frac{1}{1 + \lambda_{H3PO4} \ \frac{M_{H2O}}{M_{H3PO4}}}$$

$$w_{P2O5} = \frac{1}{1 + \lambda_{P2O5} \frac{M_{H2O}}{M_{P2O5}}}$$



3.1.2.2 PA ionic conductivity in CL

The proton conductivity of the PA is estimated from the water content according to the curve (see **Figure 12**), according to Melchior [28]:

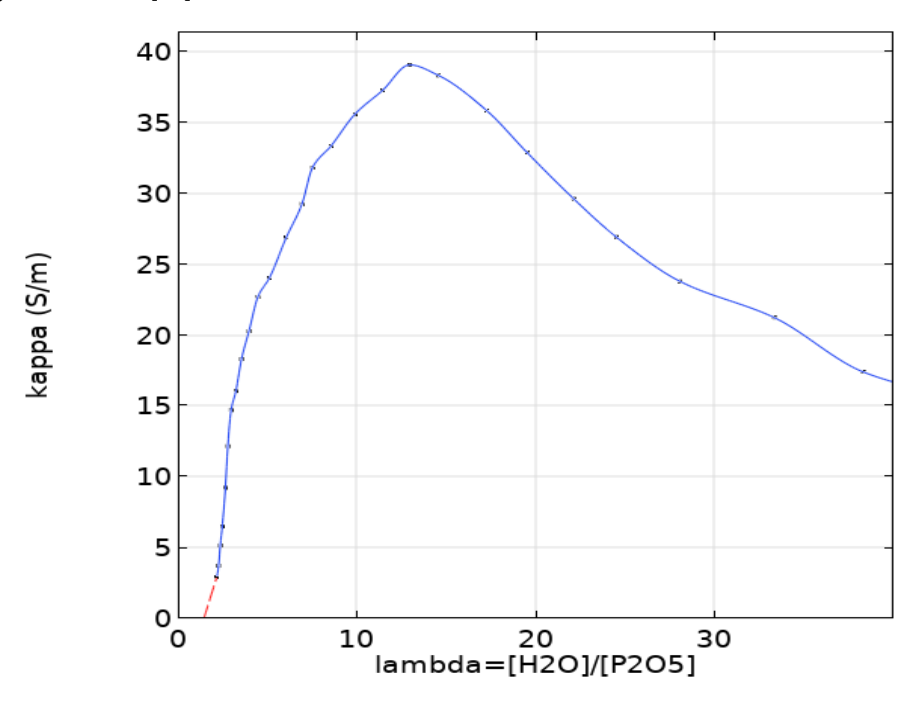


Figure 12: PA ionic conductivity as a function of water content

3.1.2.3 Diffusion and solubility of oxygen in PA

Oxygen diffusion through the PA film is calculated according to Scharifker [29]:

$$D_{O_2} = k_1 e^{-\frac{k2}{T}}$$

The coefficients were determined according to [29]:

$$k1 = 1.37 E-6 m^2/s$$

$$k2 = 2605 K$$

The solubility (Henry) is expressed as:

$$H_{O_2} = k_1 e^{k2(\frac{1}{T} - \frac{1}{298.15})}$$

With

$$k1 = 5.052 E-7 \text{ mol/m}3/Pa$$

$$k2 = 1077 K$$



3.1.2.4 Phosphoric acid adsorption in CL

The adsorption of PA in CL is taken into account with the help of θ_{H3PO4} , which is the ratio of the surface of PA adsorption sites to the Pt surface.

The surface coverage θ_{H3PO4} is used as a factor to modify (decrease) the specific surface area of Pt (Platinum rugosity) which represents the surface of Pt available for ORR divided by the electrode volume.

Let's consider

 γ_{PT} : specific surface area in m²/m³

and

 θ_{H3PO4} : surface coverage of PA

Then after adsoption:

$$\gamma_{PT}^{ad} = \gamma_{PT} \cdot (1 - \theta_{H3PO4})$$

The surface coverage θ_{H3PO4} is described experimentally according to the article [30] of P. Zelenay et al. According to the article, the evolution of PA adsorption depends on temperature and potential. The values of the article [30] are used to create a map of θ_{H3PO4} as a function of temperature and potential. The **Figure 13** is based on data from this article:

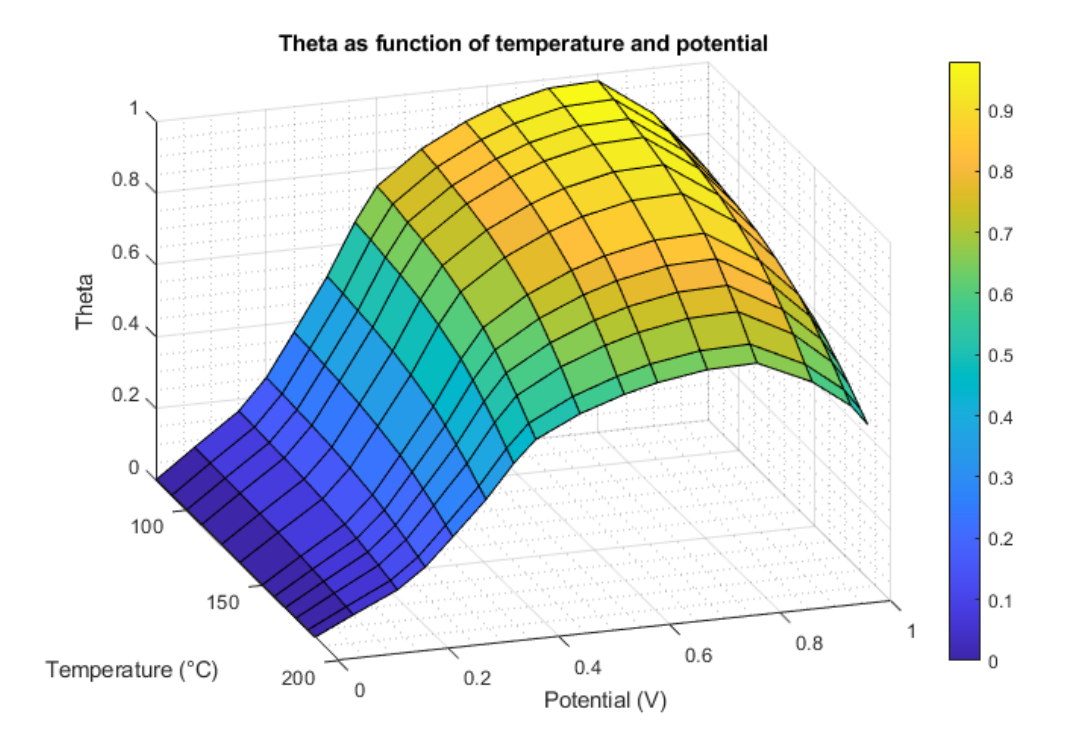


Figure 13 : Surface coverage θ_{H3PO4} as a function of T and potential

The figure shows an extremum of θ_{H3PO4} for a potential of approximately 0.8 V and a decrease of Θ with increasing temperature.



3.1.2.5 Other properties

The diffusion coefficient of water in the PA (in m²/s) and the electro-osmosis coefficient were also updated:

$$D_{H20} = 4.66 \, . \, 10^{-10} \, \lambda - 8.66 \, . \, 10^{-10}$$

$$a_{eo} = -0.037(\lambda - 3)(\lambda - 12.1)$$
, if $\lambda > 3$

The thickness of the PA film covering the catalyst needs to be estimated. This can be done from the volume fraction of acid in the acid + carbon phase and the specific surface area of carbon.

$$e_{H3PO4} = \frac{(1 - \epsilon)\epsilon_{H3PO4}}{\gamma_{carbon}}$$

The acid fraction is recalculated from the initial dry fraction and water content so as to fill the pores without modifying the solid phase (carbon):

$$\epsilon_{H3PO4} = \frac{r_{H3PO4} \epsilon_{H3PO4}^{dry}}{1 + (r_{H3PO4} - 1) \epsilon_{H3PO4}^{dry}}$$

where r_{H3PO4} is the PA swelling ratio as a function of water content:

$$r_{H3PO4} = 1 + \frac{2}{3}\lambda_{H3PO4}$$

The pore radius of the CL is also recalculated, assuming that as the acid swells with water, it invades the pores uniformly:

$$R_p = R_p^{dry} \left(\frac{\epsilon}{\epsilon^{dry}}\right)^{1/3}$$

where the porosity ϵ of the CL is calculated according to :

$$\epsilon = 1 - (1 - \epsilon^{dry})(r_{H3PO4} + \epsilon^{dry}_{H3PO4}(1 - r_{H3PO4}))$$



4 Calibration of the model parameters

4.1 Calibration methodology

Calibrations are carried out using experimental data on differential cells: A6334-SAMP5562.

These experimental data are made by CEA with ADVENT PBI membrane based MEA.

The operating conditions below are applied as a function of:

Temperature, Relative humidity, Pressure, H₂ and O₂ fractions.

The following table resumes the OC.

OC	T(°C)	RH (%)	P (bar)	XX_H2	XX_O2
1	160	0	1	1	0.21
2	160	0	1	0.2	0.21
3	160	0	2.5	1	0.21
4	180	0	2.5	1	0.21
5	180	0	1	1	0.21
6	180	0	1	0.2	0.21
7	180	2	1	1	0.1
8	180	2	2.5	1	0.1
9	180	2	1	0.2	0.1
10	160	3	1	0.2	0.1
11	160	3	1	1	0.1
12	160	3	2.5	1	0.1
13	160	0	1	1	0.21
14	120	5	1	1	0.15
15	160	0	1	1	0.21
16	160	3	1.18	1	0.21
17	160	5	1.3	1	0.21
18	160	10	1.46	1	0.21

Table 2: Experimental design for differential cell testing

The EuROPIUM model is generally calibrated using differential cell tests. This makes it possible to avoid 'inlet/outlet' heterogeneities depending on the direction of gas flow and to work with MEA models in cross-section perpendicular to the channels. The high stoichiometry ratios inherent in differential cell operation mean that there is very little variation in gas composition (hydrogen fraction, oxygen, relative humidity) between the cell inlet and outlet. Similarly, because the active surface area is small compared with the thickness of the bipolar and clamping plates, cooling and temperature can be considered to be homogeneous.

Consequently, the current density is uniform over the cell surface and the boundary conditions are known at the channel level.

In principle, a calibration procedure involves the following steps. These steps may be modified according to the input data in our possession and any simulation difficulties encountered.



4.1.1 Step 0

Before embarking on calibration, it is helpful to specify as completely as possible everything that is known or supposed to be known: GDL properties (some data is sometimes supplied by the manufacturer), thickness of components (membrane, active layer), sorption isotherm if available, etc.

4.1.2 Step 1

If reliable high-frequency resistance measurements are available, we can begin by calibrating the proton resistance of the membrane. This calibration assumes that the other purely ohmic losses (contact resistances and GDL+MPL electrical resistances) are known, as well as the thickness and sorption isotherm of the membrane. The principle is to adjust the coef_kappa_* parameters that determine the membrane conductivity as a function of its water loading.

<u>Note</u>: Calibration to the high-frequency resistances is carried out by a transient numerical simulation of the model using a high-frequency signal as input. The advantage of this compared with a more analytical method is that it reproduces the experiment numerically as faithfully as possible and integrates conductivity heterogeneities in the thickness or plane of the different materials.

4.1.3 Step 2

To reduce the number of parameters to be calibrated, polarisation curves are generally only used at low current densities (typically up to a maximum of 0.1 to 0.3A/cm²). This eliminates gas transport parameters, which have no effect on the start of the polarisation curve. It is also recommended that you do not necessarily use all the curves available, but try to separate the effects and associated parameters. For example, an initial calibration can be carried out using only the curves at a given temperature and relative humidity to focus on the influence of the hydrogen and oxygen fractions. This approach limits the time needed to obtain an initial calibration of certain model parameters and reduces the risk of the optimisation algorithm getting blocked in a local minimum. It is also easier to analyse the results and compare them with experiments on a reduced number of curves.

4.1.4 Step 3

The next step is to take more polarisation curves into account. For example, use the curves at 2 temperature levels and for several gas hydration levels. This stage is always carried out at low current density to try to decouple the phenomena as far as possible, by separating the calibration of the electrochemical and electrical parameters from the calibration of the parameters affecting the transport of the reactants.

4.1.5 Step 4

The next step is to calibrate the transport parameters: mainly the tortuosity of the porous media (GDL, MPL, CL), but we generally also come back to the diffusion of gases through the ionomer. For this step, the entire polarisation curve must be used, as in principle it is the points at low potential (high current) that are sensitive to transport (the so-called 'diffusion limit'). The calibration is therefore carried out by scanning the polarisation curves in potential and comparing the currents (calculated and experimental) rather than the other way round, as the achievable current density depends on the experimental conditions for each curve.

4.1.6 Notes

Note 1: The model is calibrated on the polarisation curves using a quasi-stationary simulation (with a current or voltage sweep). The transient or hysteresis effects observed experimentally and (suspected of being) linked to temperature, water loading of the ionomer, oxide formation or other phenomena are therefore not taken into account. A decision has to be made on the basis of the experimental results whether to take into account the 'forward' curve (increase in current), the 'return' curve (decrease in current) or an average of the two, as the differences are sometimes significant.



<u>Note 2</u>: The calibrations in the following paragraphs (4.2 and 4.3) do not show the various stages previously described, but summarise the calibrations obtained at the time of publication of this deliverable.

<u>Note 3</u>: These calibrations are open to improvement and do not represent final results. They will be improved in the course of the studies.

4.2 Calibration of ECP and transport parameters

The table below summarises the parameters taken into account for these calibrations The values are coming from the fitting of the experimental data with the model.

Table 3: List of calibration parameters coming from fitting of the experimental data with the model – EC and transport

Parameter name	Value example	Description
dHox0_a	1.103 [J/mol]	Enthalpy of formation of the activated
		complex (in the oxidation direction) _ anode
dSox0_a	-273.623[J/(mol*K)]	Entropy of formation of the activated complex
		(in the oxidation direction) _ anode
dHox0_c	1.383e+05 [J/mol]	Enthalpy of formation of the activated
		complex (in the oxidation direction) _ cathode
dSox0_c	-61.239[J/(mol*K)]	Entropy of formation of the activated complex
		(in the oxidation direction) _ cathode
alpha_a	0.517	Anode charge transfer coefficient
alpha_c	0.001	Cathode charge transfer coefficient
gamma_H2	1.367	Order of reaction relative to hydrogen
gamma_O2	-1.954	Order of reaction relative to oxygen
gamma_H2O	-0.261	Order of reaction relative to water
coef_Hh_naf_A	8 e-4[mol/m³/Pa]	
coef_Hh_naf_B	0	Henry law coefficients for H ₂
coef_Hh_naf_T	1920[K]	
coef_Ho_naf_A	2 e-5[mol/m³/Pa]	
coef_Ho_naf_B	0.002	Henry law coefficients for O ₂
coef_Ho_naf_T	1464[K]	
coef_Dh_naf_A	9.6e-13[m ² /s]	
coef_Dh_naf_B	-0.003	Diffusion coefficients for H ₂
coef_Dh_naf_T	3241[K]	
coef_Do_naf_A	9.783 e-11[m²/s]	
coef_Do_naf_B	0.006	Diffusion coefficients for O ₂
coef_Do_naf_T	4238[K]	
tor_CL	1.791	CL tortuosity
tor_naf_CL	0.550	Ionomer tortuosity in CL
tor_GDL	2.270	GDL tortuosity

In the model, the OCV depends on the hydrogen permeation current and the cathodic reaction kinetics. The parameters likely to affect it are: dHox0_c, dSox0_c, alpha_c, gamma_O2, gamma_H2O, and coef_Dh_naf_*_MB.

In the last part of the polarisation curve, typically when the cell voltage falls below 0.5V or less, transport phenomena become predominant. This part of the curve will therefore be affected by the diffusion of the reactants through the porous media (GDL, MPL, CL) and through the ionomer of the active layer. The parameters to be considered are the tortuosities and the coefficients determining the absorption and transport of reactants through the ionomer: coef H* naf *, coef D* naf *.



Because of the large number of points and curves, it is difficult to identify a simulated curve that is far from the corresponding experimental results. This is why we use a representation that compares the simulated voltage and the experimental voltage for a fixed current density (it is also possible to fix the voltage and compare the current densities). Each point corresponds to a manipulation. The aim is to have a cloud of points as close as possible to the X=Y line.

The results below correspond to the voltages for the following current densities: 0.05A/cm² (**Figure 14**), 0.5A/cm² (**Figure 15**) and 1 A/cm² (**Figure 16**).

dHox0_a=1.1025 dHox0_c=138365.4595 dSox0_a=-273.623 dSox0_c=-61.2392 alpha_a=0.5169 alpha_c=0.001 gamma_H2=1.367 gamma_O2=-1.954 gamma_H2O=-0.26081 coef_Dh_naf_A_MB=2.1616e-12 coef_Dh_naf_B_MB=-0.0024932 coef_Dh_naf_T_MB=4580.5838 coef_Do_naf_A_MB=9.7825e-11 coef_Do_naf_B_MB=0.0061885 coef_Do_naf_T_MB=4283.3894 coef_Hh_naf_A_MB=0.0061807 coef_Hh_naf_T_MB=1920.9043 coef_Hb_naf_A_MB=2.4607e-095 coef_Ho_naf_B_MB=0.001807 coef_Ho_naf_T_MB=1463.8096 coef_Dh_naf_A_CL_a=9.558e-13 coef_Dh_naf_B_CL_a=-0.026766 coef_Dh_naf_T_CL_a=3241.3355 coef_Do_naf_A_CL_c=2.9075e-10 coef_Do_naf_B_CL_c=0.008025 coef_Do_naf_T_CL_c=1102.0547 coef_Hh_naf_A_CL_a=0.0063858 coef_Hh_naf_B_CL_a=4.1351e-05 coef_Hh_naf_T_CL_a=2785.2243 coef_Ho_naf_A_CL_c=0.0059256 coef_Ho_naf_T_CL_c=1102.0547 coef_Hn_naf_T_CL_c=0.0059256 coef_Ho_naf_T_CL_c=1.3586 tor_CL_c=1.7913 tor_naf_CL_a=0.33958 tor_naf_CL_c=0.55002 tor_GDL_c=2.27

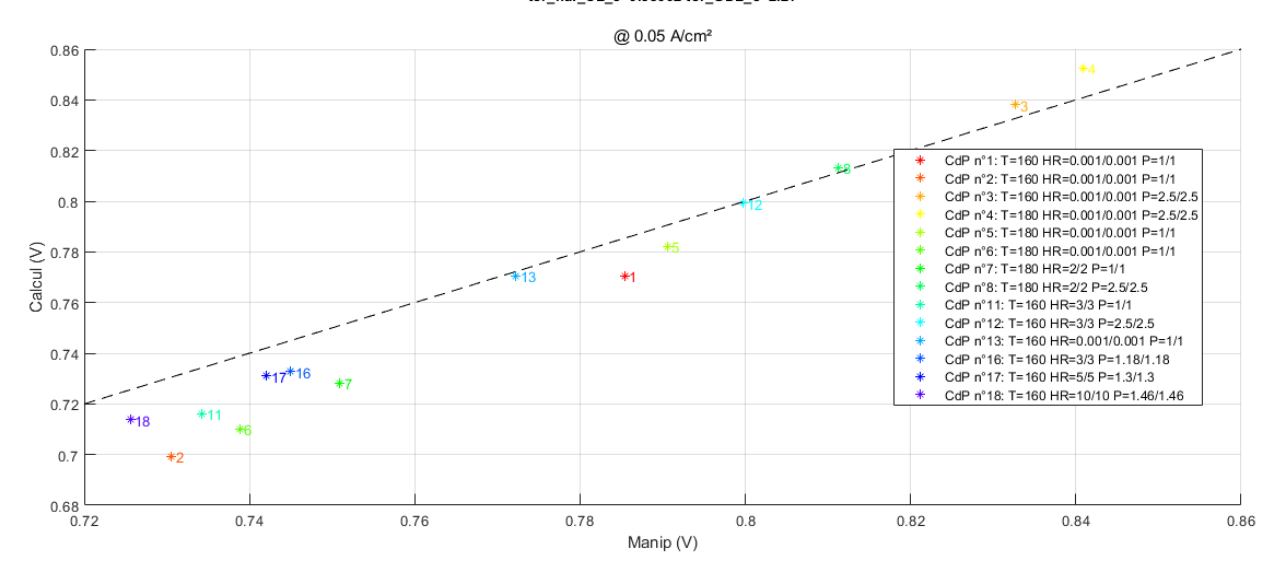


Figure 14: Experimental voltage vs. measured voltage @ 0.05 A/cm²

The simulation results are relatively close to the experimental results, and we are almost within the order of magnitude of the reproducibility of the tests (especially if we take into account the hysteresis generally observed experimentally). The larger deviations at very low current density can be explained by the fact that the polarization curves are very steep in this zone: a small deviation in current very quickly leads to a large deviation in voltage.



dHox0_a=1.1025 dHox0_c=138365.4595 dSox0_a=-273.623 dSox0_c=-61.2392 alpha_a=0.5169 alpha_c=0.001 gamma_H2=1.367 gamma_O2=-1.954 gamma_H2O=-0.26081 coef_Dh_naf_A_MB=2.1616e-12 coef_Dh_naf_B_MB=0.0024932 coef_Dh_naf_T_MB=4580.5838 coef_Do_naf_A_MB=9.7825e-11 coef_Do_naf_B_MB=0.0061885 coef_Dn_naf_T_MB=4238.3984 coef_Hh_naf_A_MB=0.0061807 coef_Hh_naf_B_MB=0.0061807 coef_Ho_naf_T_MB=1403.8096 coef_Dh_naf_A_CL_c=9.558e-13 coef_Dh_naf_B_CL_a=-0.026766 coef_Dh_naf_T_CL_a=3241.3355 coef_Do_naf_A_CL_c=2.9075e-10 coef_Do_naf_B_CL_c=0.008025 coef_Do_naf_T_CL_c=1102.0547 coef_Hh_naf_A_CL_a=0.0063858 coef_Hh_naf_B_CL_a=4.1351e-05 coef_Hh_naf_T_CL_a=2785.2243 coef_Ho_naf_A_CL_c=0.005025 coef_Ho_naf_B_CL_c=0.005025 coef_Ho_naf_B_CL_c=0.0050255 coef_Ho_naf_CL_c=0.0050256 coef_Ho_naf_B_CL_c=0.0050256 coef_Ho_naf_CL_c=0.0050256 coef_Ho_

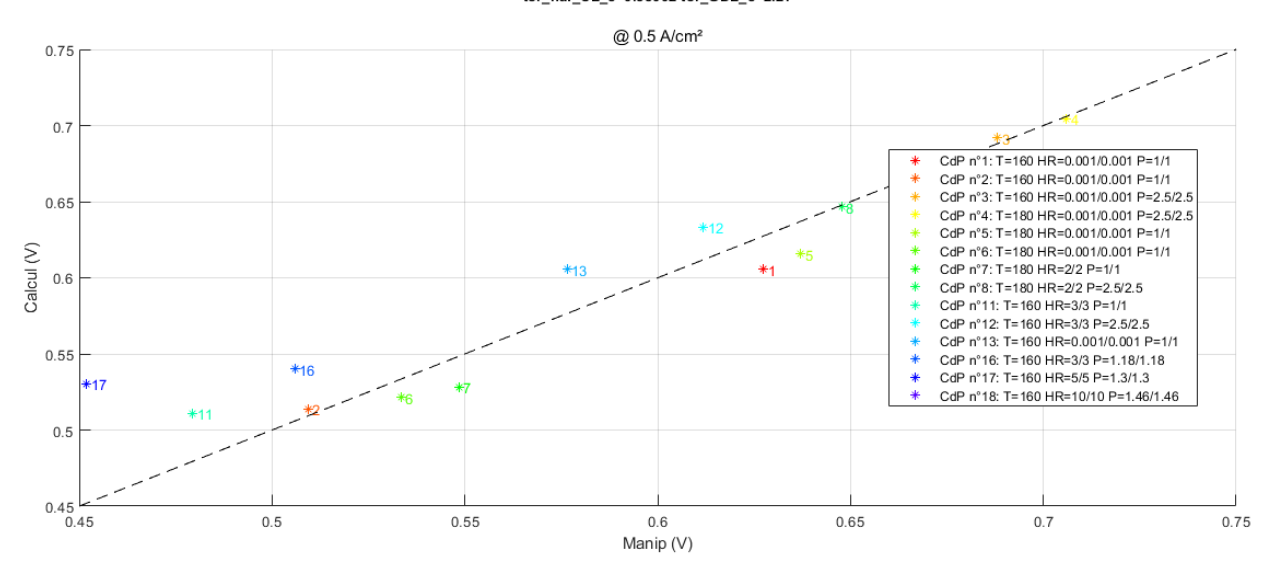


Figure 15: Experimental voltage vs. measured voltage @ 0.5 A/cm²

In most cases, the simulated results are close to the measured results.

dHox0_a=1.1025 dHox0_c=138365.4595 dSox0_a=-273.623 dSox0_c=-61.2392 alpha_a=0.5169 alpha_c=0.001 gamma_H2=1.367 gamma_O2=-1.954 gamma_H2O=-0.26081 coef_Dh_naf_A_MB=2.1616e-12 coef_Dh_naf_B_MB=-0.0024932 coef_Dh_naf_T_MB=480.5838 coef_Do_naf_A_MB=9.7825e-11 coef_Do_naf_B_MB=-0.001885 coef_Do_naf_T_MB=4233.3894 coef_Hh_naf_A_MB=0.00618302 coef_Hh_naf_B_MB=0 coef_Hh_naf_T_MB=1920.9043 coef_Hb_naf_A_MB=2.4607e-05 coef_Ho_naf_B_MB=0.001807 coef_Ho_naf_T_MB=1463.8096 coef_Dh_naf_A_CL_a=9.558e-13 coef_Dh_naf_B_CL_a=-0.026766 coef_Dh_naf_T_CL_a=3241.3355 coef_Do_naf_A_CL_c=2.9075e-10 coef_Do_naf_B_CL_c=0.008025 coef_Do_naf_T_CL_c=1102.0547 coef_Hh_naf_A_CL_a=0.00063858 coef_Hh_naf_B_CL_a=4.1351e-05 coef_Hh_naf_T_CL_a=2785.2243 coef_Ho_naf_A_CL_c=3.3568e-07 coef_Ho_naf_B_CL_c=0.0059256 coef_Ho_naf_T_CL_c=1.726.534 tor_CL_a=1.3586 tor_CL_c=1.7913 tor_naf_CL_a=0.33958 tor_naf_CL_c=0.55002 tor_GDL_c=2.27

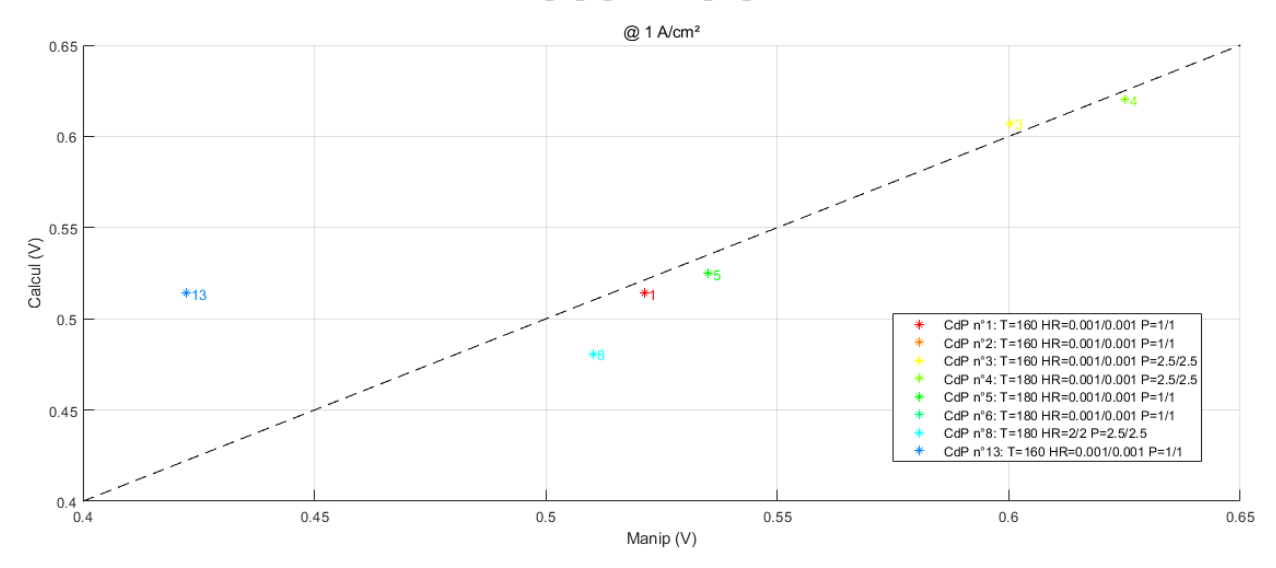


Figure 16: Experimental voltage vs. measured voltage @ 1 A/cm²

There are fewer points at 1A/cm² because not all conditions allow this current density to be achieved. For the points reached, there is good agreement between the manipulator and the model, with the exception of point 13, which presents the same OC as point 1 (consequently, the simulations results are identical).



4.3 Calibration of membrane ionic conductivity parameters

The table below summarises the parameters taken into account for these calibrations:

Table 4: List of calibration parameters – membrane ionic conductivity

Parameter name	Value example	Description
coef_kappa_ld1_MB	508[S/m]	
coef_kappa_ld2_MB	0.8	Coefficients for calculating ionic conductivity
coef_kappa_ld3_MB	-6	
coef_kappa_T_MB	5000[K]	

The effects are cumulative, so the calibration of the linear part of the polarisation curve also depends on the parameters influencing the start of the curve. However, we can hope to better adjust this part of the curve without affecting the start of the curve too much by adjusting the conductivity of the membrane.

The main parameters are the coef_kappa_*_MB, which calculates the membrane conductivity as a function of temperature and water loading (see section 3.1.1).

The results below are given for all the experimental results in the differential cell.

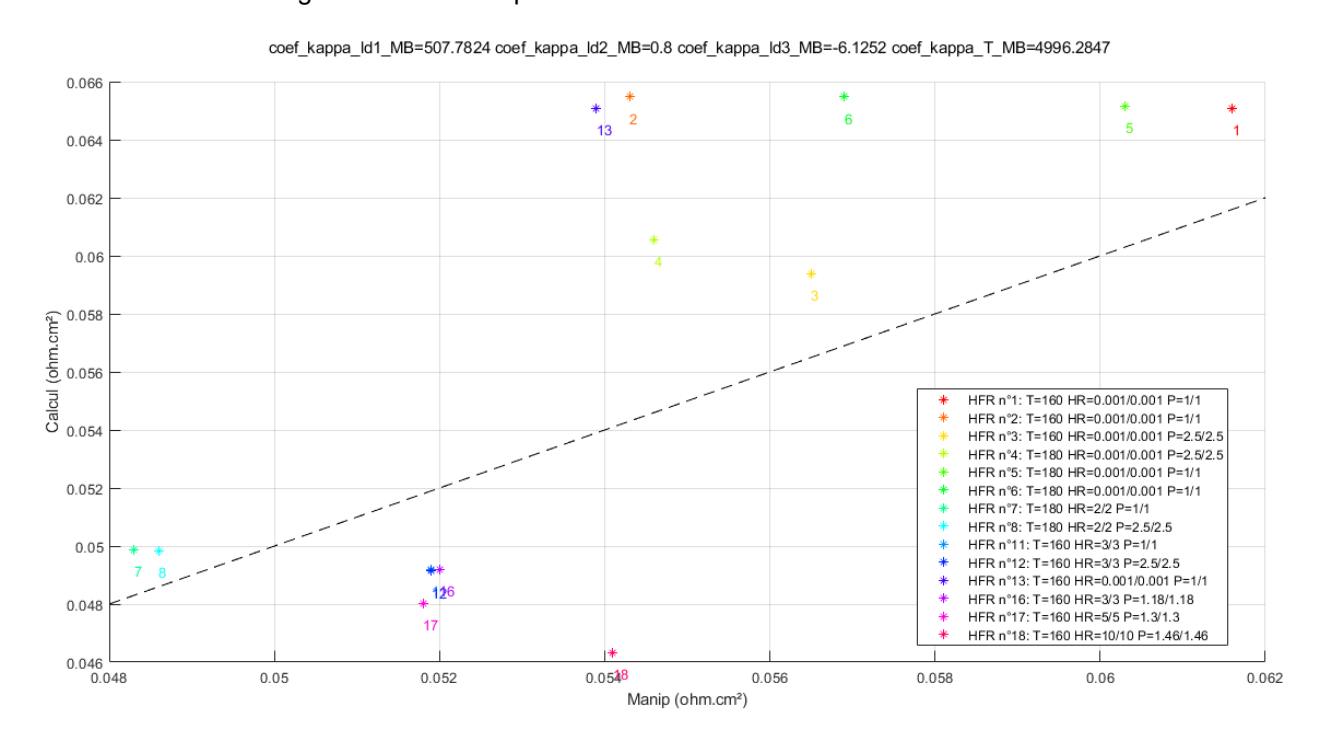


Figure 17: Measured ohmic resistance vs simulated ohmic resistance

It can be seen that the results deviate from the X=Y line, which reflects the algorithm's difficulty in finding a set of parameters that allow the experimental results to coincide with the numerical results for all the operating conditions.

For the extreme case (OC n°2), we note a difference of around 0.01 ohm.cm², i.e. a voltage difference of around 10 mV at 1 A/cm². This difference for the extreme case remains reasonable.



5 Presentation of first results

The results presented in this paragraph are based on the simulation of OC n°4, which gives the best performance of all OCs.

It represents a case at the highest temperature (180° C), pressure (2.5 bar), H₂ and O₂ fractions (1 and 0.21) and the lowest RH (nearly zero).

The results of the other conditions can also be used for the purposes of the project.

5.1 I-V curve

The following figure shows the simulated polarisation curve for OC n°4 and compares it with the experimental results.

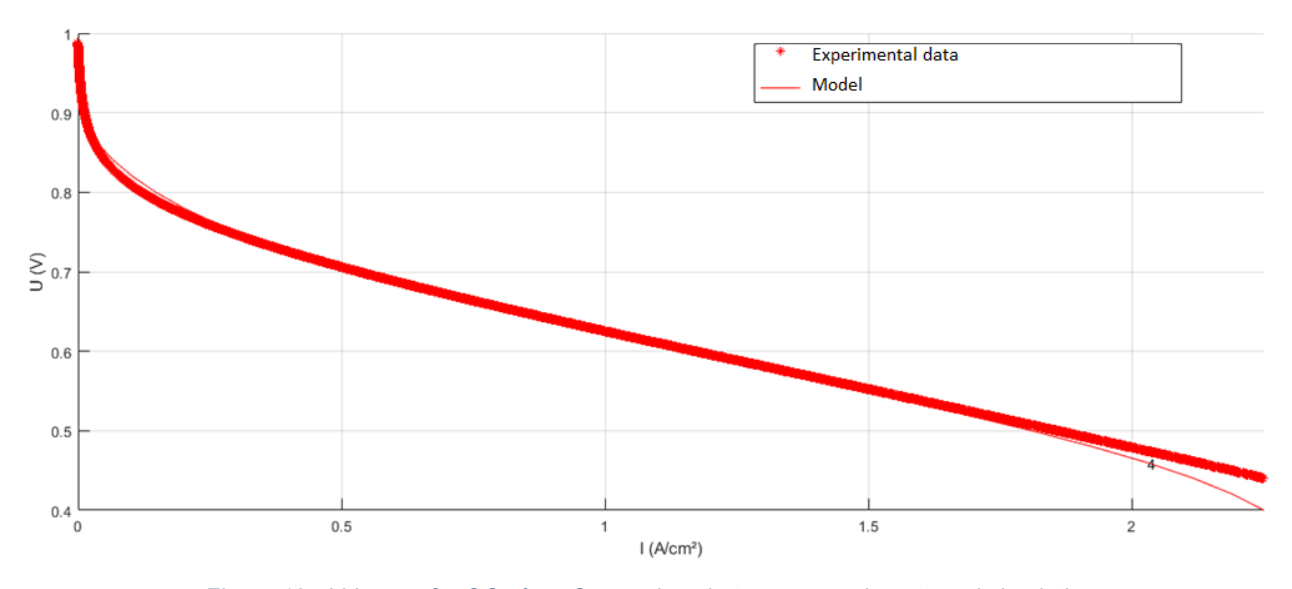


Figure 18: I-V curve for OC n°4 - Comparison between experiments and simulation

It can be seen that the simulated linear part (ohmic loss) is perfectly comparable with the experimental results.

There is a very slight difference in the first part of the polarisation curve (activation losses).

At very high current densities (approximately 2 A/cm²), differences in diffusion limitations begin to appear.

<u>Note</u>: the calibration used to obtain this curve is not specific to OC 4 but includes the compromises necessary for the other OCs. We can assume that these compromises do not allow us to obtain the most accurate parameters for tortuosity or oxygen diffusion coefficients, for examples.



5.2 Some results

5.2.1 RH

The following figure shows the evolution of relative humidity in the MEA as a function of potential.

The results in the **Figure 19** are centered on the membrane, with part of the MEA on the <u>cathode side on the left</u> and the <u>anode side on the right</u>.

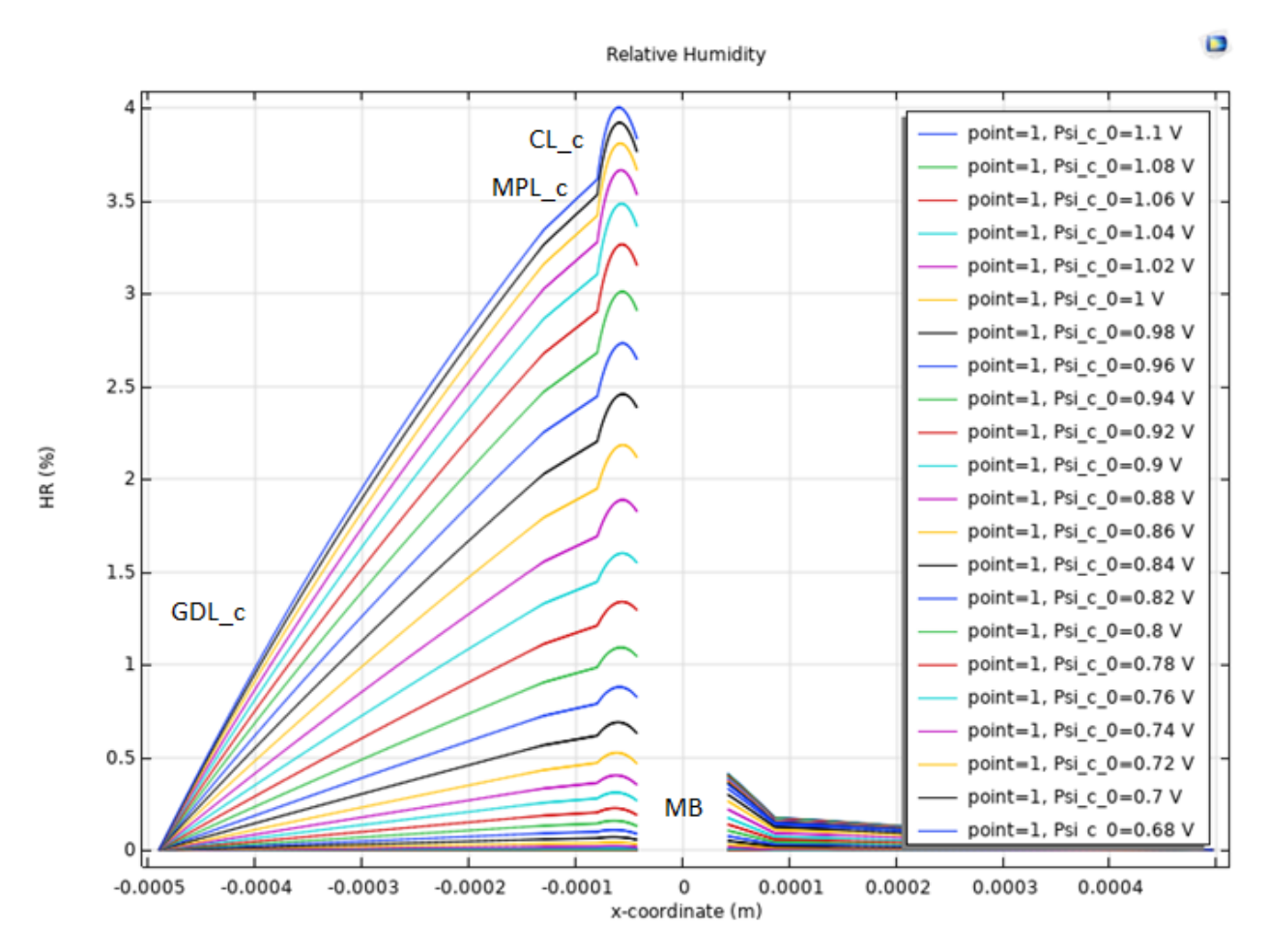


Figure 19: Evolution of RH in the MEA

The results show higher RHs at the cathode because of the production of water at the cathode.

Note:

In the following figures, the color codes of the legends correspond to the same potentials shown in the previous figure. The legends have been removed for clarity.



5.2.2 Water content

The following figure shows the evolution of water content as a function of potential.

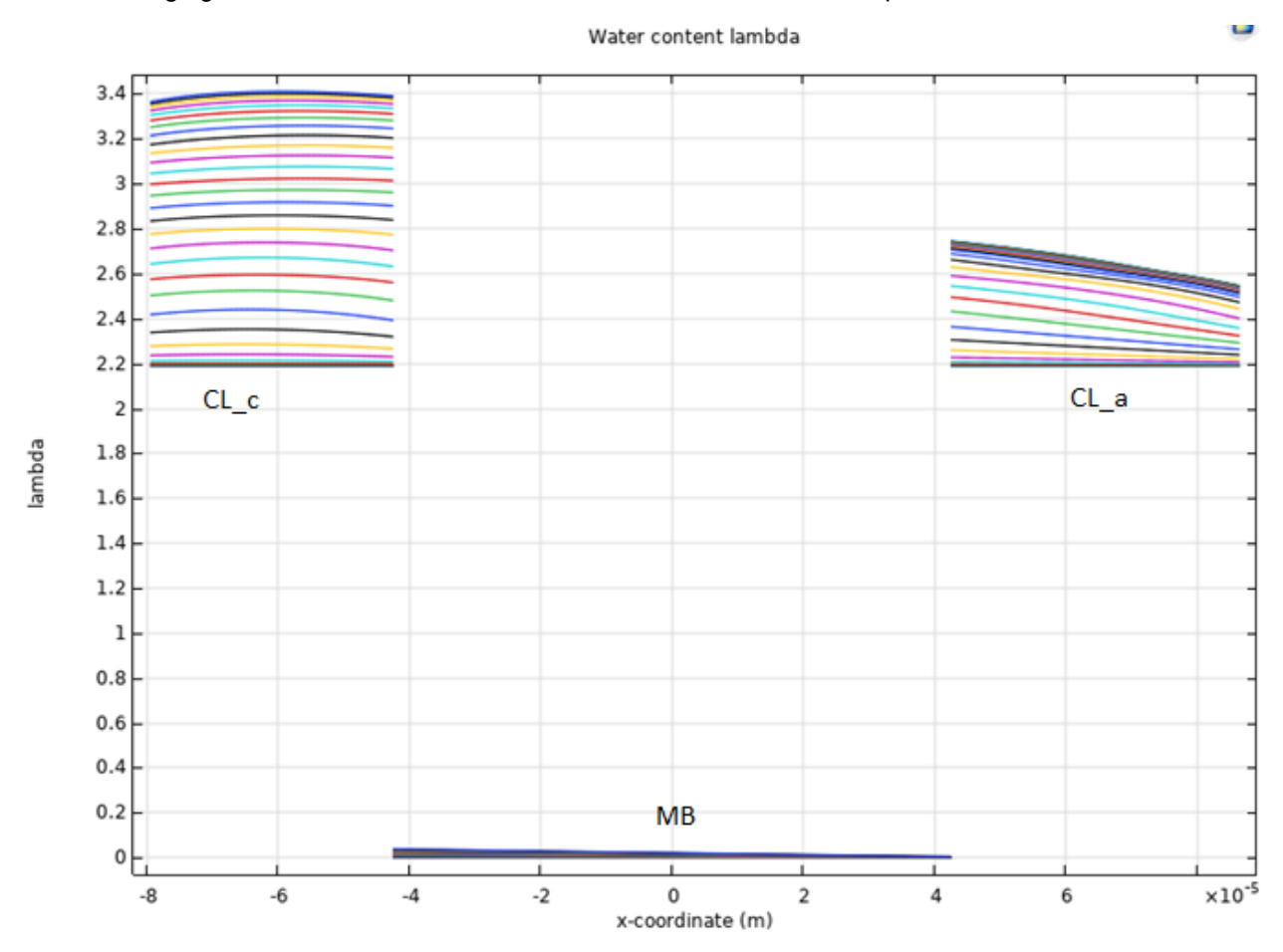


Figure 20 : Evolution of water content λ in CL and MB

The **Figure 20** shows the evolution of the water content in the active layers (anode on the right and cathode on the left) and in the membrane (center).

<u>Note</u>: The water content in the membrane is not comparable because its definition is different (in the membrane lambda = HR/100 and in the CL as per section 3.1.2.1).



5.2.3 CL effective conductivity

The following figure shows the evolution of CL effective conductivity as a function of potential.

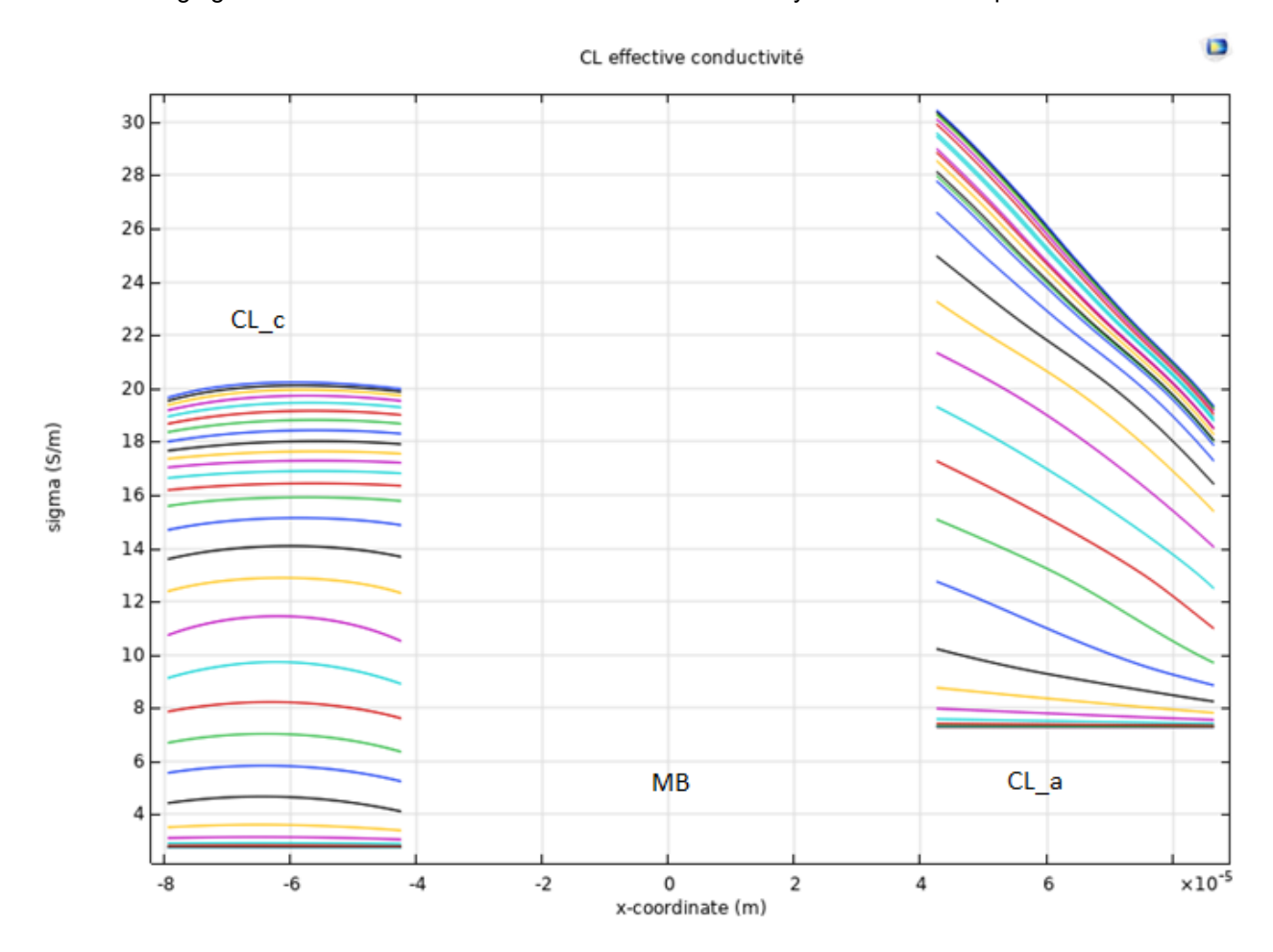


Figure 21: Evolution of CL effective conductivity

It can be seen that the conductivity profiles at the cathode are relatively homogeneous due to an approximately constant water content (**Figure 20**), while at the anode the profiles decrease towards the GDL, following the same trend as the water content (**Figure 20**).



5.2.4 Electronic potential

The **Figure 22** and **Figure 23** show the electronic potential on the cathode side and the anode side as a function of potential.

Note: the scales are not identical.

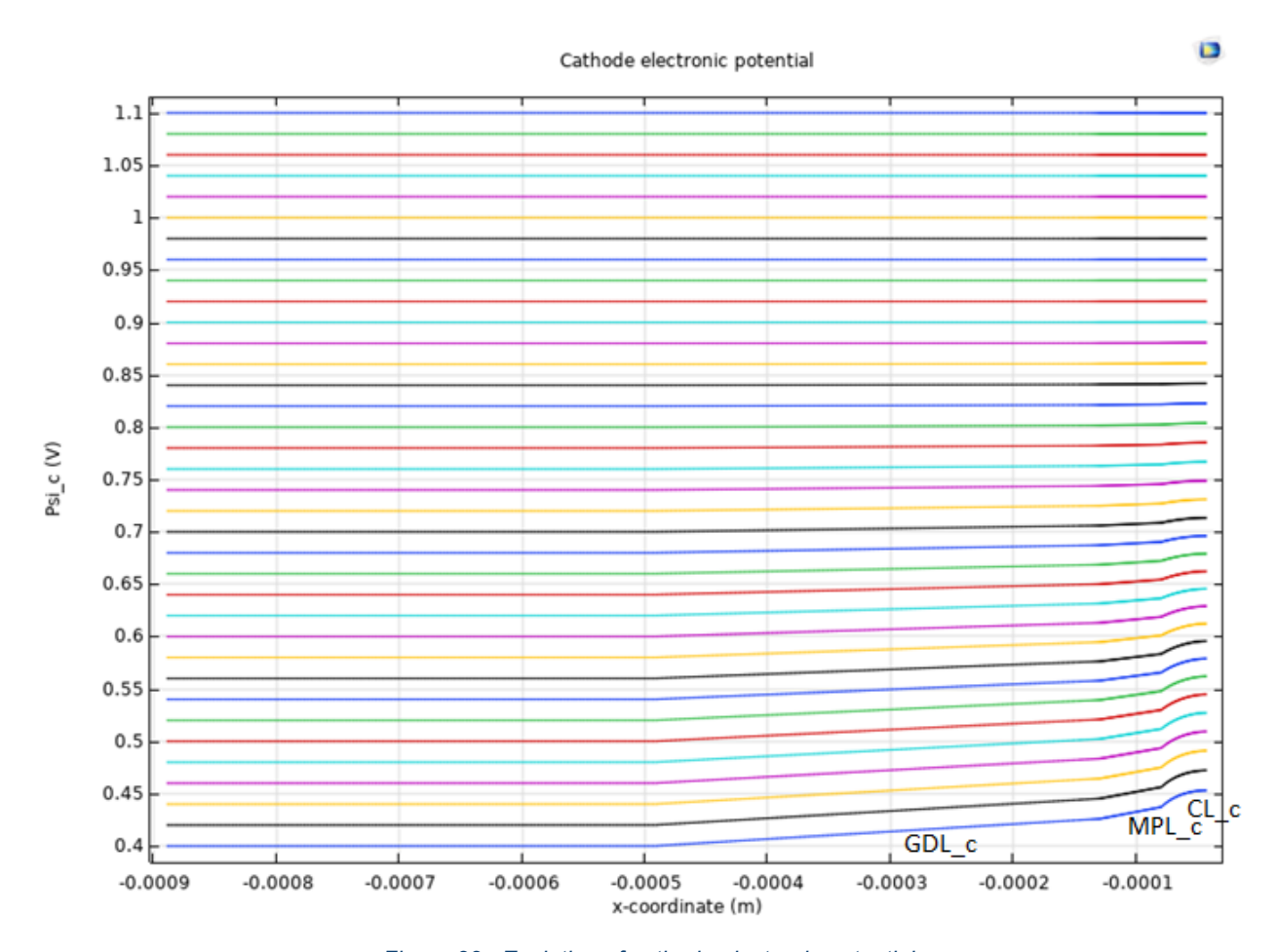


Figure 22: Evolution of cathode electronic potential



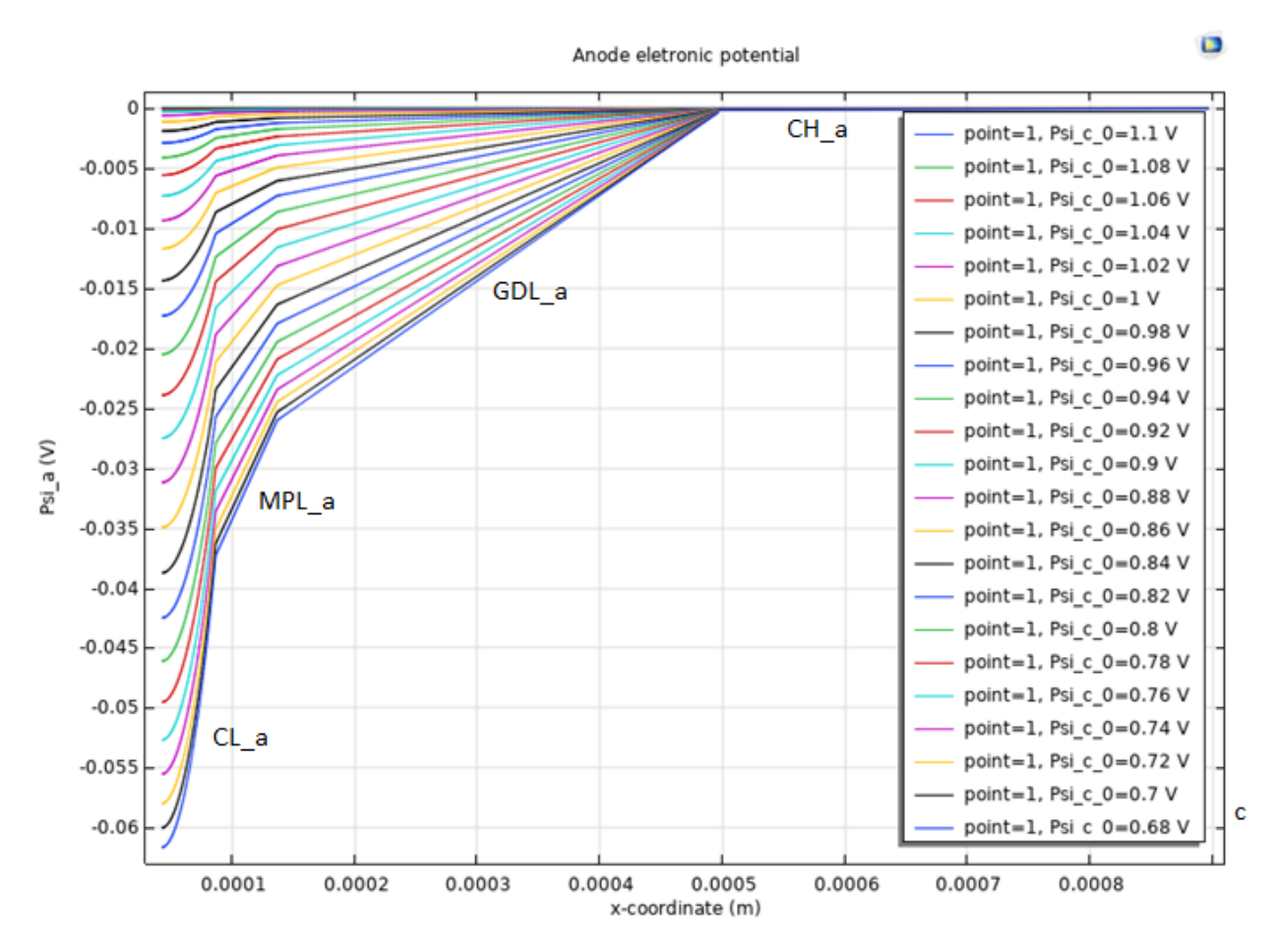


Figure 23: Evolution of anode electronic potential

At the cathode, it can be seen that the Ohmic losses are mainly in the catalyst layer. At the anode, there are also losses at the GDL, but losses at the catalyst layer are not negligible.

On both side the Ohmic losses are comparable: of 40 mV/A/cm².



5.2.5 Ionic potential

The Figure 24 shows the evolution of ionic potential in CL cathode, membrane and CL anode.

It emphasizes the ionic losses that occur on the CLs.

The calibration parameters for the conductivity of the PBI membrane (see section 3.1.1) induce ionic losses close to zero at the membrane. This point will need to be confirmed during the later parts of the project and adapted to the new types of membranes explored within NIMPHEA.

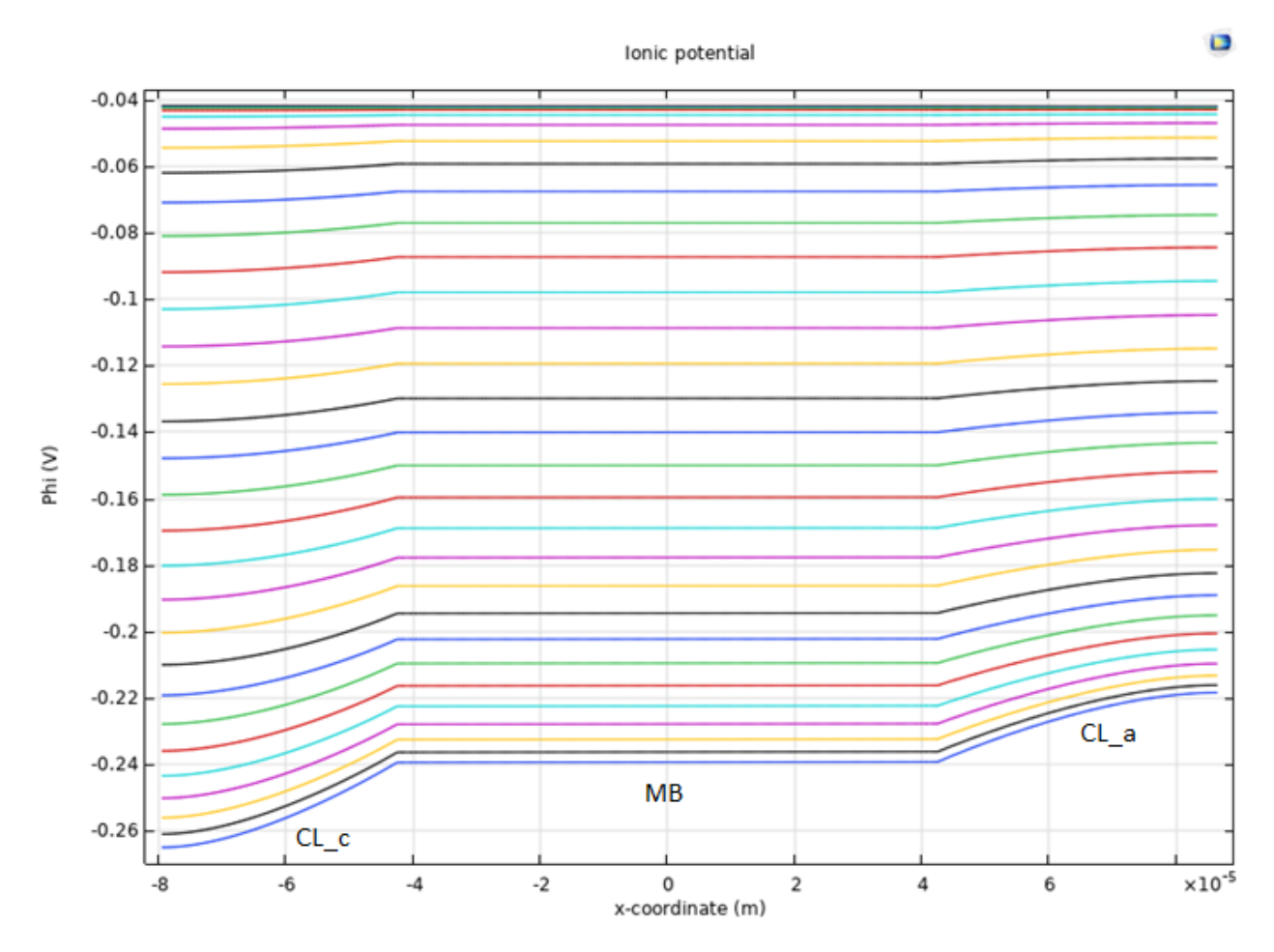


Figure 24: Evolution of ionic potential in the MEA



5.2.6 Overpotential

Figure 24 and **Figure 25** show the evolution of the overpotential and the local current density at the cathode and anode.

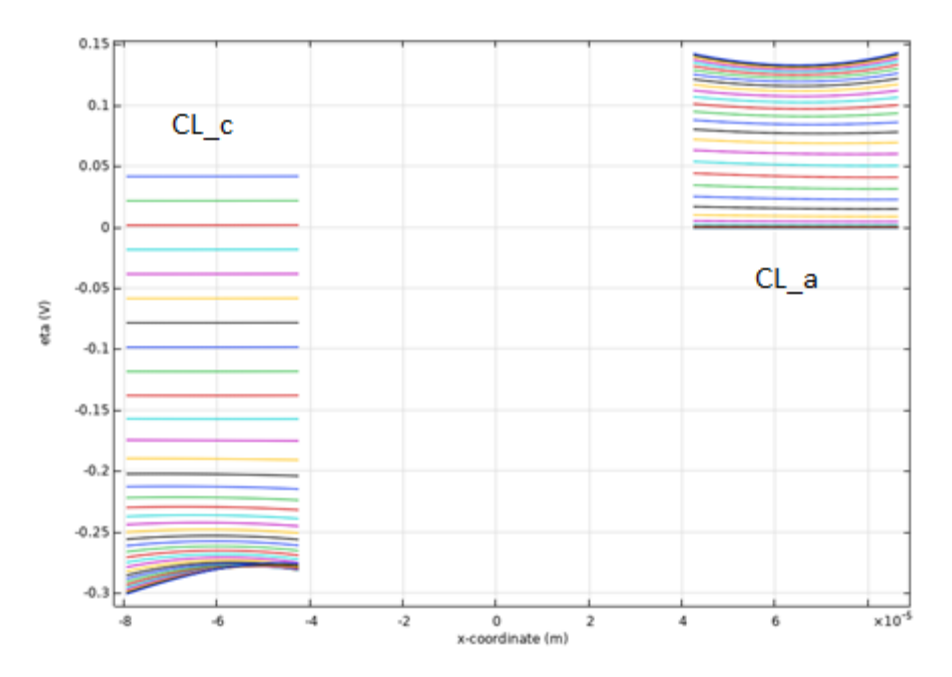


Figure 25: Evolution of overpotential at the CL cathode and CL anode

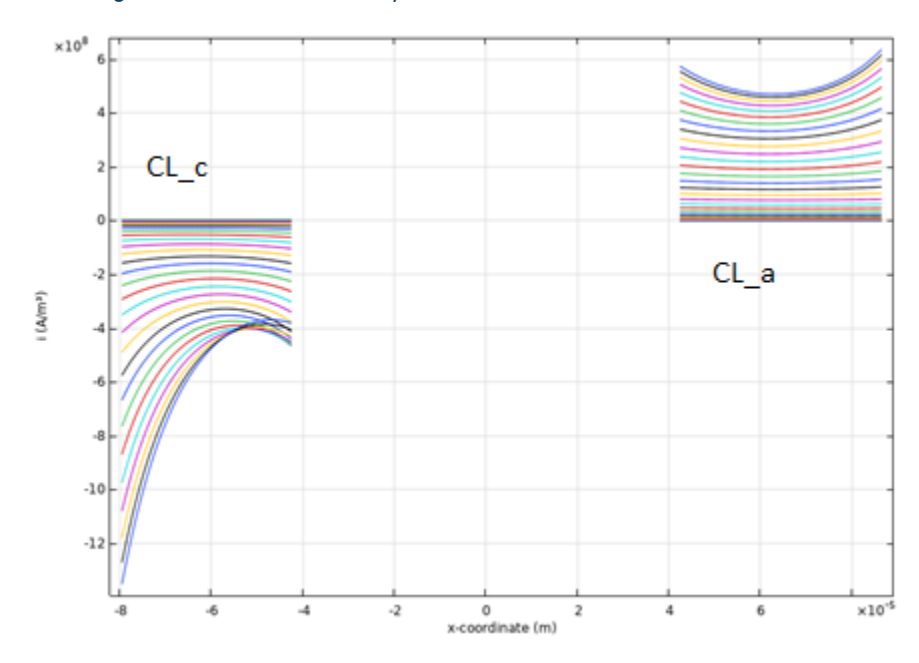


Figure 26: Evolution of local current density at the CL cathode and anode

It can be seen that the overpotential is higher at the cathode (where the ORR is located).

Also, we can see that the local current density is not uniform throughout the thickness of the CLs.



5.3 PEIS simulation

The **Figure 24** and **Figure 25** show the impedance spectrum for case CO n°4 with the previously calculated parameters.

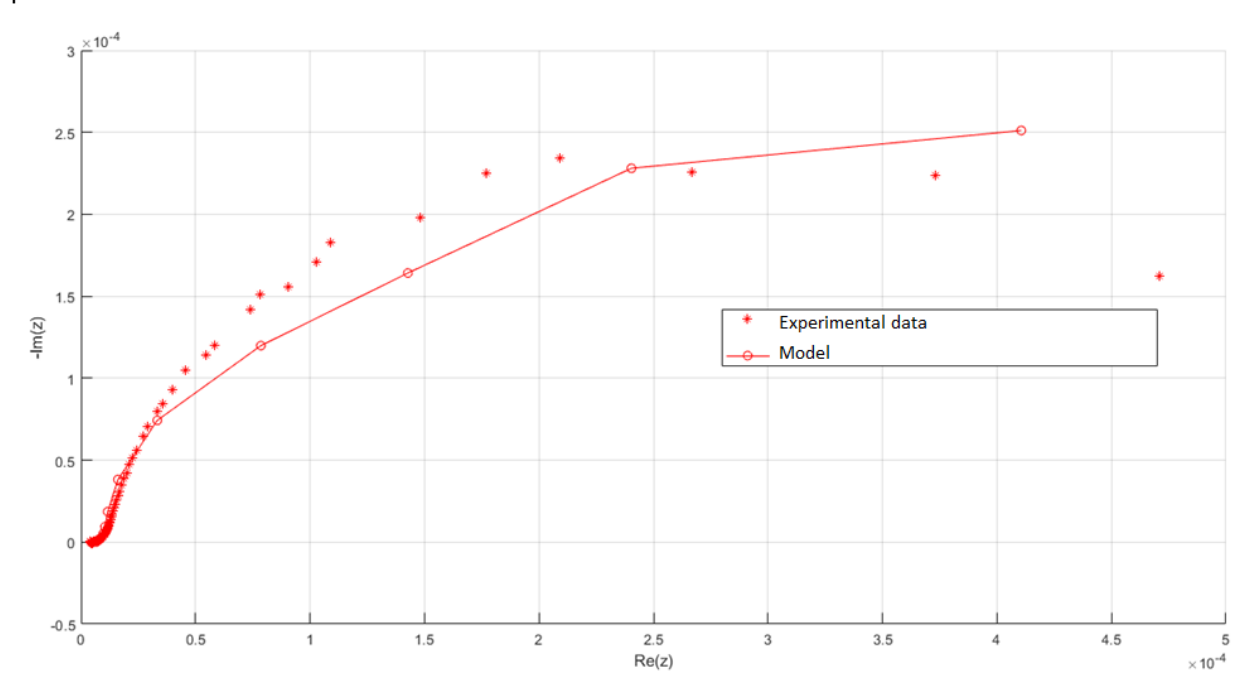


Figure 27: Impedance spectrum - CO n°4

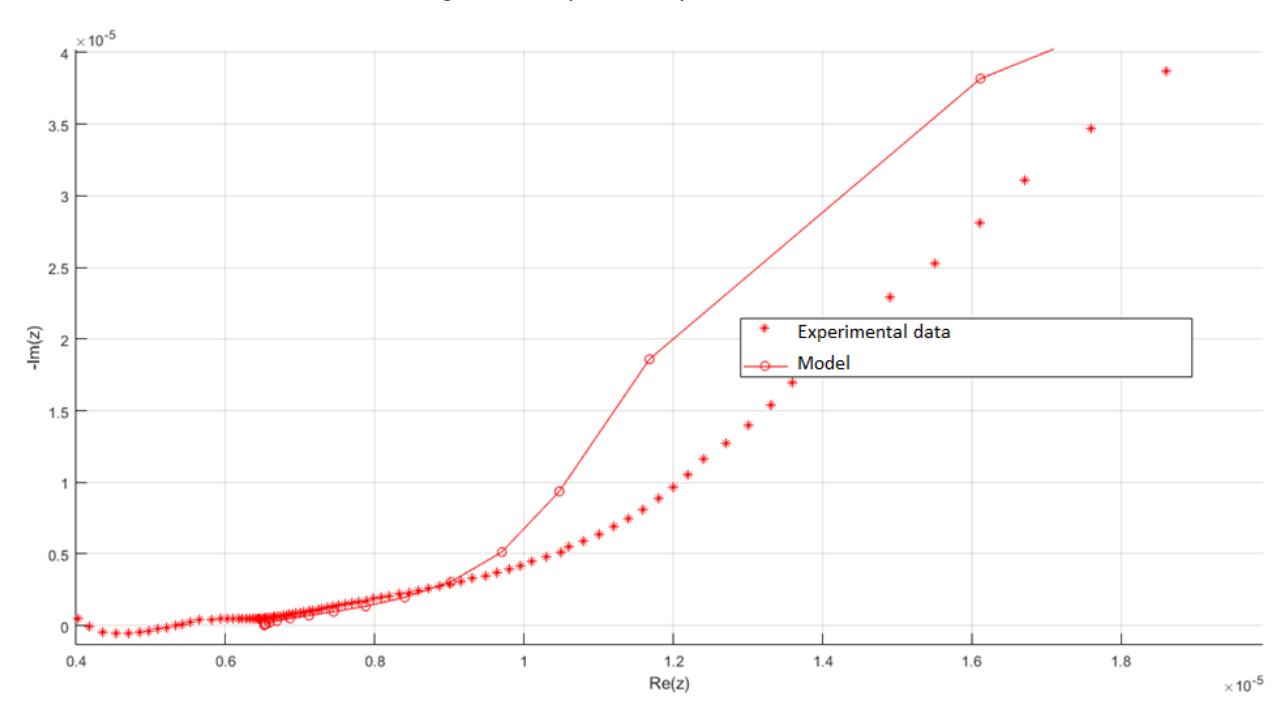


Figure 28: Partial enlargement of the high frequency region

The simulated spectrum represents the measured spectrum reasonably well, especially in the high-frequency region, thanks to the HFR calibration that was carried out in section 4.3.



6 Conclusion and perspectives

The EuROPIUM models were adapted for this project.

Specificities of PBI membranes and membranes containing phosphoric acid were added and a calibration procedure was set up in order to reproduce the available experimental results.

The parameters obtained with the AME_1D models will be fed into the 2D models (rib-channel and channel) to enable more detailed simulations.

These simulations will make it possible to analyse performance losses, by analysing, for example, ionic potential maps or exchange current density distribution, and so forth.

Results at variable temperatures, RH, etc. should help to analyse the experimental results and better identify the causes of performance losses.

Finally, the models will be used to predict performance at representative OC to help in cell design.



7 Bibliography

- [1] Randrianarizafy, B., Schott, P., Chandesris, M., Gerard, M. and Bultel, Y. 2018. Design optimization of rib/channel patterns in a PEMFC through performance heterogeneities modelling. *International Journal of Hydrogen Energy*. 43, 18 (2018), 8907–8926.
- [2] Bird, R.B., Stewart, W.E. and Lightfoot, E.N. 1960. Transport Phenomena. Wiley International Edition.
- [3] Fick, A. 1855. Über Diffusion. Annalen der Physik und Chemie. 94, (1855), 59–86.
- [4] Knudsen, M. 1909. Die Gesetze der Molekularströmung und der inneren Reibungsströmung der Gase durch Röhren. Annalen der Physik. 333, 1 (1909), 75–130.
- [5] Krishna, R. and Wesselingh, J.A. 1997. The Maxwell-Stefan approach to mass transfer. Chemical Engineering Science. 52, 6 (1997), 861–911.
- [6] Runstedtler, A. 2006. On the modified Stefan-Maxwell equation for isothermal multicomponent gaseous diffusion. Chemical Engineering Science. 61, 15 (2006), 5021–5029.
- [7] Young, J.B. and Todd, B. 2005. Modelling of multi-component gas flows in capillaries and porous solids. International Journal of Heat and Mass Transfer. 48, 25-26 (2005), 5338–5353.
- [8] Kudo, K., Jinnouchi, R. and Morimoto, Y. Humidity and Temperature Dependences of Oxygen Transport Resistance of Nafion Thin Film on Platinum Electrode. 209, 682–690.
- [9] Meier, F. and Eigenberger, G. 2004. Transport parameters for the modelling of water transport in ionomer membranes for PEM-fuel cells. *Electrochimica Acta*. 49, 11 (2004), 1731–1742.
- [10] Zawodzinski, T.A., Davey, J., Valerio, J. and Gottesfeld, S. 1995. The water content dependence of electroosmotic drag in proton-conducting polymer electrolytes. *Electrochimica Acta*. 40, 3 (1995), 297–302.
- [11] Zawodzinski, T.A., Derouin, C., Radzinski, S., Sherman, R.J., Smith, V.T., Springer, T.E. and Gottesfeld, S. 1993. Water Uptake by and Transport Through Nation 117 Membranes. J. Electrochem. Soc. 140, 4 (1993), 1041–1047.
- [12] Zawodzinski, T.A., Neeman, M., Sillerud, L.O. and Gottesfeld, S. 1991. Determination of water diffusion coefficients in perfluorosulfonate ionomeric membranes. *J. Phys. Chem.* 95, 15 (Jul. 1991), 6040–6044.
- [13] Wang, C.-Y. and Beckermann, C. 1993. A two-phase mixture model of liquid-gas flow and heat transfer in capillary porous media - I. Formulation. *International Journal of Heat and Mass Transfer*. 36, 11 (1993), 2747– 2758.
- [14] Barbir, F. 2013. PEM Fuel Cells (Second Edition). Academic Press.
- [15] Kudo, K. and Morimoto, Y. Analysis of Oxygen Transport Resistance of Nafion Thin Film on Pt Electrode. 50, 2,
- [16] Hussaini, I.S. and Wang, C.Y. 2010. Measurement of relative permeability of fuel cell diffusion media. *Journal of Power Sources*. 195, 12 (2010), 3830–3840.
- [17] Robin, C. 2015. Développement d'un modèle prédictif de durée de vie d'une pile PEMFC pour une application aéronautique: étude des interactions entre le coeur de pile et les conditions d'opération du système. INPG.
- [18] Epstein, N. 1989. On tortuosity and the tortuosity factor in flow and diffusion through porous media. *Chemical Engineering Science*. 44, 3 (1989), 777–779.
- [19] Agaësse, T. 2016. Simulations des transports monophasiques et diphasiques dans des microstructures poreuses à partir d'images tomographiques de couches de diffusion des gaz de piles à combustible à membrane échangeuse de protons. Institut de Mécanique des Fluides de Toulouse.
- [20] Robin, C., Gerard, M., d Arbigny, J., Schott, P., Jabbour, L. and Bultel, Y. 2015. Development and experimental validation of a PEM fuel cell 2D-model to study heterogeneities effects along large-area cell surface. *Int. J. Hydrogen Energy*. 40, 32 (2015), 10211–10230.
- [21] Gerbaux, L. 1996. Modélisation d'une pile à combustible de type hydrogène/air et validation expérimentale. INPG.



- [22] Poirot-Crouvezier, J.-P. 2000. Modélisation dynamique des phénomènes hydrauliques, thermiques et électriques dans un groupe électrogène à pile à combustible destiné à l'application automobile. INPG.
- [23] Satterfield, M.B. and Benziger, J.B. Non-Fickian Water Vapor Sorption Dynamics by Nafion Membranes. 112, 12, 3693–3704.
- [24] Nernst, W. 1889. Die elektromotorische Wirksamkeit der Jonen. Zeitschrift für physikalische Chemie. 4, 1 (1889), 129–181.
- [25] Nernst, W. 1889. Über gegenseitige Beeinflussung der Löslichkeit von Salzen. Zeitschrift für physikalische Chemie. 4, 1 (1889), 129–181.
- [26] Shaposhnik, V.A. 2008. Walter Nernst and analytical chemistry. Journal of Analytical Chemistry. 63, 2 (Feb. 2008), 199–201.
- [27] Schott, P. 2016. Quelques réflexions sur le potentiel thermodynamique, les enthalpies de réactions et de changement de phase.
- [28] Melchior, J.-P., Kreuer, K.-D. and Maier, J. 2017 Proton conduction mechanisms in the phosphoric acid-water system (H4P2O7-H3PO4.2H2O): a 1H, 31P and 17O PFG-NMR and conductivity study. *Phys. Chem. Chem. Phys.* 19, 1 (2017), 587-600.
- [29] Scharifker, B.R., Zelenay, P. and Bockris, J.O. 1987. The Kinetics of Oxygen Reduction in Molten Phosphoric Acid at High Temperatures. *Journal of The Electrochemical Society*. 134, 11 (Nov. 1987), 2714-2725.
- [30] Zelenay et al 1986 J. Electrochem. Soc. 133 2262